Journal of
Materials Chemistry C

REVIEW

View Article Online
View Journal | View Issue

Cite this: J. Mater. Chem. C, 2019, 7, 13709

Tunable nanofibril heterojunctions for controlling interfacial charge transfer in chemiresistive gas sensors

Shuai Chen, *[ab] Nan Gao, [a] Benjamin R. Bunes[bc] and Ling Zang *[b]

Chemiresistive sensors, particularly those based on nanostructures, have drawn increasing attention for application in security and environmental monitoring, healthcare, biomedicine and others due to their high selectivity and sensitivity in detection of gaseous chemicals. Nanofibers possess large surface area, and exhibit unique electronic and optical properties that arise from their one-dimensional (1D) structures. They are an ideal candidate for development as sensors, even when constructed into heterojunction structures between n-type (electron acceptor) and p-type (electron donor) materials. Nanofibril heterojunctions created are highly tunable for enhancing the interfacial charge separation and transfer by modifying and optimizing both the material electronic structures and interface configuration spacing. This review aims to provide a comprehensive overview of the current state of the art of chemiresistive gas sensors based on nanofibril heterojunctions, with special focus on the control of interfacial charge transfer which is critical to the sensor performances. Various nanofibril heterojunction structures, including inorganic metal oxides, carbon materials, conjugated organic molecules, and functional polymers, are summarized. The properties of precisely tunable interfaces are discussed, in conjunction with the sensor mechanisms. The potential limitations and challenges of these exciting materials and heterojunction structures for further sensor enhancement and real-world application are also discussed. Lastly, an outlook is given on the future directions of developing nanofibril heterojunction sensors. This review will not only provide deep understanding of the structural design of nanofibril heterojunctions, and the interfacial charge transfer and chemiresistive sensor mechanisms, but also lay out more potential for extending them to other electronic and optoelectronic applications.

Received 23rd August 2019,
Accepted 4th October 2019

DOI: 10.1039/c9tc04659c

rsc.li/materials-c

[a] School of Pharmacy, Jiangxi Science & Technology Normal University, Nanchang 330013, Jiangxi, China. E-mail: shuai.chen@utah.edu; Fax: +1 801-581-4816; Tel: +1 801-587-1551
[b] Nano Institute of Utah and Department of Materials Science and Engineering, University of Utah, Salt Lake City 84112, Utah, USA. E-mail: lzang@eng.utah.edu
[c] Vaporsens Inc., 615 Arapeen Drive, Suite 102, Salt Lake City, Utah 84108, USA

Shuai Chen

Shuai Chen is a professor hired by Jiangxi Science & Technology Normal University, P. R. China. He earned his PhD degree (2015) in materials physics and chemistry from the University of Chinese Academy of Sciences, and since 2018 has been a postdoctoral fellow with Prof. Ling Zang at the University of Utah. His current research emphasizes the design and fabrication of new functional semiconductor nanocomposites for chemosensors or photocatalytic energy transfer, as well as intrinsically conducting polymer films with flexibility and self-healing capability for optoelectronic applications.

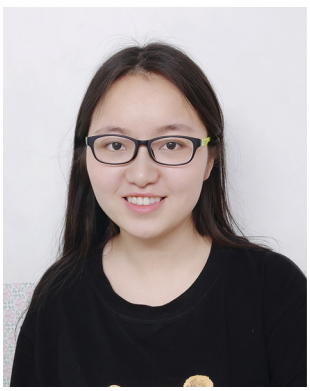

Nan Gao

Nan Gao graduated in the major of chemistry from Zhoukou Normal University, P. R. China, and now is a master's student under the supervision of Dr Shuai Chen in Jiangxi Science & Technology Normal University. She focuses on the research of fabricating flexible organic electrodes based on nanofibril composites, and exploring self-healing thin-films of intrinsic conducting polymers as well as their uses in organic electronic devices.

1. Introduction

Interfacial charge transfer (ICT) is a critical process for realizing and controlling the optoelectronic features of photovoltaics (PVs), field-effect transistors (FETs), light-emitting diodes (LEDs), photodetectors, fuel cells, photo-/photoelectro-catalysis, biosensors/chemical sensors, fluorescence imaging, and other electronic devices. Chemiresistive sensors (CRSs) have attracted wide attention in the fields of environmental quality, safety, healthcare, disease diagnosis, space exploration, and others.[1–15] These fields require sensors to monitor trace gaseous chemicals such as NO_x, NH_3, H_2S, SO_2, CO, H_2, and hazardous or toxic volatile organic compounds (VOCs), with sensitivities ranging from parts per million (ppm) or parts per billion (ppb) to even parts per trillion (ppt).[16–19] Chemiresistive detection established in all-solid-state devices is the most appropriate technique for portable and personalized sensors due to its simple operation principle and configuration, through real-time changes in one of the simplest and most cost-effective electrical signals (current I or resistance R) upon interaction with reducing or oxidizing or inert gaseous analytes.[12] The key requirements and ever-present challenges of a perfect CRS are to achieve comprehensive performance such as high sensitivity, good selectivity, a low detection limit, short response/recovery times, low energy consumption, non-severe operating conditions, good repeatability, durability, and others.[5] Sensing materials and ICT processes within themselves and from adsorbed gas molecules to their exposed surfaces play the primary roles in maintaining the performances of CRSs.

At present, common active materials for sensors employed in this field are inorganic metal oxide semiconductors (MOSs) including some chalcogenides,[9–13,16,17] nonmetallic carbon materials, including single-walled or multi-walled carbon nanotubes (SWCNTs or MWCNTs),[1,14,15,18] and graphenes like reduced graphene oxide (RGO),[7,8] and intrinsically conducting polymers (ICPs).[3–6] However, the real applications of CRSs still face many issues, such as insufficient detection limits, poor selectivity to distinguish analytes between chemicals, and poor manufacturing reproducibility, especially when using a single material system.[9,10] With regard to these issues, tailoring conventional materials into nanostructures with morphological versatility like one-dimensional (1D) nanofibers and fabricating tunable hybrid composites like p–n heterojunctions are being pursued. They can be seen as two widely used and preferred paths to modulate optoelectronic devices including CRSs.[20–27] Thus, during the last decade, researchers in this field have paid tremendous attention to the fabrication of nanofibril heterojunctions exhibiting unique advantages.

Nanofibril heterojunctions offer several features that are attractive to CRSs. (1) Intrinsically unique features of 1D nanofibers. (a) Large aspect ratios and high surface area-to-volume ratios compared with those of the bulk phase, open microporosity, and continuous or hierarchical nanofibril networks preserving their high density in comparison with common compact films lead to a high capacity to adsorb gaseous analytes, facilitating gas diffusion and fast response times.[1] (b) Their nanoscale size facilitates enhanced surface activity for surface adsorption/desorption of targeted gaseous analytes.[3] (c) Arising from the small cross-sectional area of nanofibril materials, quantum effects and orientated conduction along the 1D axial direction, the capability to fabricate long charge carrier transport channels leads to fast reaction speed and maximal current response (in other words, short response time and high sensitivity).[5,7] (d) The high degree of crystallinity and large planar facets also reduce lattice mismatch that can be found in conventional two-dimensional (2D) thin-films and thus improve sensitivity, and provide additional high long-term stability compared to nanoparticles, which have been widely investigated by researchers.[22] However, it should be noted that these three-dimensional (3D) porous architectures, special surfaces, and charge transfer properties may lead to

Benjamin R. Bunes

Benjamin R. Bunes is the Director of Research and Development of Vaporsens, Inc. He holds a PhD in Materials Science and Engineering from the University of Utah. He has been involved in research surrounding nanotechnology/nanomaterials for thirteen years, with the past ten years focused on nanomaterial sensors for chemical detection. He was previously a NASA Space Technology Research Fellow and an ASEE/NSF Small Business Postdoctoral Research Diversity Fellow.

Ling Zang

Ling Zang is a professor at the University of Utah, affiliated with the Department of Materials Science and Engineering, and the Nano Institute of Utah. He received his PhD in chemistry from the Chinese Academy of Sciences. He was previously an Alexander von Humboldt Fellow at Erlangen-Nuremberg University in Germany, an NSF CAREER Award winner, and a K. C. Wong Foundation Research Fellow. His current research focuses on nanoscale imaging and molecular probing, organic semiconductors and nanostructures, optoelectronic sensors and nanodevices, with the long-term goal of achieving real applications in the areas of national security, health monitoring, renewable energy, and clean environments.

relatively moderate recovery times and poor selectivity. (2) Hybrid or heterostructures. (a) Combining the advantages of two or more dissimilar components and forming inter-/intramolecular heterojunctions can facilitate ICT and interfacial reactions, improving sensitivity and selectivity, operation at lower operating temperatures, and low limits of detection.[6,22,24] (b) Some special multi-dimensional architectures such as brush-like nanofibers, 2D nanosheet decorated 1D nanofibers, core@shell structures, and hollow nanotubes have large specific surface areas.[25] (c) Nanofibers can be easily manipulated, facilitating device miniaturization with high integration density, less power consumption and low cost, as well as requiring only a small concentration of gaseous analytes, *i.e.*, low detection limit.[5] (d) Individual sensors can be integrated into dense arrays, enabling simultaneous detection of multiple analytes.[5,27] Therefore, in comparison to single semiconductors or other types of composites, nanofibril heterojunction materials could be ideal candidates for high-performance CRSs and have been in immense demand.

In these aspects, in recent years, related fields have witnessed rapid development indicated by extensive excellent review papers on 1D nanostructures or nanoscale homojunctions/heterojunctions and their related optoelectronic applications, especially transistors, photovoltaics, and chemical and biological sensors mainly employing MOSs,[8,10,13,17,20,24–28] and fewer on ICPs,[4,6] SWCNTs,[14,15] and PTCDI assemblies.[21,29] This work is presented to fulfill the need for a systematic review of the remarkable advances of nanofibril heterojunction CRSs and precise control of their interfaces for improved charge transfer properties, especially that employ inorganic–organic and organic–organic architectures. Thus, in view of the rapid progress in the last decade, we believe it is crucial to provide a deep, systematic review specifically focusing on all three aspects: nanofibril structure, heterojunction, and ICT mechanism in CRSs, pushing forward their future development.

First, a concise introduction of the tunable structures and design philosophy of nanofibril heterojunctions for controlling charge transfer and separation behavior in diverse optoelectronic devices and CRSs for gas detection is presented. Then, a detailed discussion about the current state of the art of inorganic/inorganic, inorganic/organic and organic/organic nanofibril heterojunctions, mainly employing MOSs, ICPs, or molecular assemblies with different morphologies and architectures follows. The prime roles and mechanisms of tunable nanofibril heterojunctions in controlling ICT behaviors in conjunction with the performances of CRSs discussed in detail. Finally, we give a brief outlook with some new insights into the future of this topic, particularly in light of recent progress in the fields of flexible sensors and integrated sensor arrays.

2. Nanofibril heterojunctions for controlling charge transfer and separation in optoelectronic systems

Since there are many special reviews focusing on nanoscale heterojunctions related to optoelectronic applications,[26–28,30–33] only a basic picture covering the popular inorganic and organic materials for forming diverse nanofibril structures will be presented.

The most familiar representative is the n–p type heterojunction, which is the basis for most optoelectronic devices.[26,34–42] Diverse fabrication methods such as solution-processing, vapor deposition, hard/soft templating, and templateless (*e.g.*, electrospinning) methods have been widely utilized and discussed.[27] In each architecture, a build-in-electric field created across their interfaces leads to effective separation and rapid transport along the 1D pathways of charge carriers.[13]

As an example, recently, an n–p type ZnO/NiO nanofibril heterojunction was constructed into uniformly aligned arrays (Fig. 1a) for self-powered and ultraviolet photodetectors because of the formation of photo-generated carriers accompanied by the photovoltaic effect and separated at the interface.[34] Similar n–p type heterojunctions have been explored for photoelectrocatalytic water-splitting in the form of a core/shell $WO_3/BiVO_4$ nanofibril photoanode on a F-doped TiO_2 (FTO) substrate (Fig. 1b).[35]

In contrast to most common pure inorganic materials, organic semiconductor nanofibers show advantages such as facile structural diversity at the molecular level that can be aligned with abundant physiochemical, optical, electronic and biochemical features. These advantages make pure organic or hybrid inorganic/organic heterojunction nanofibers become important competitors. In this respect, ICPs and molecular assemblies attract the most attention. Since their discovery (awarded the 2000 Nobel Prize for Chemistry) in 1977, a surge of research effort has been directed towards the development of well-known polyaniline (PANI), polypyrrole (PPy), polythiophene (PT), poly(3,4-ethylenedioxythiophene) (PEDOT), and their derivatives in optoelectronic fields.[5,6] Relying on a noted ''doping/dedoping'' process, they present p-type semiconducting characteristics (sometimes, n-type for PANI and PEDOT), exhibiting modulated electrical conductivities ranging from 10^{-10} to 10^3 S cm^{-1}. As they have typical p-type semiconductor character containing an sp^2 structure that permits delocalized transport of charge carriers when exposed to redox chemicals or another semiconductor, removing electrons leaves the polymer backbone charged and the cation radical acts as a charge carrier.[3] Unlike MOSs, ICP nanofibers exhibit intrinsic polymer mechanical flexibility, tunable electrochemical activity and biocompatibility, which make them suitable for constructing promising functional nanocomposites in optoelectronic and biomedical areas. In 2018, Zhang *et al.* overviewed the fabrication approaches of typical nanostructured ICPs and various applications of their nanocomposites.[36]

Nevertheless, precise control of the dimensions and morphology at the nanoscale and the electrical conductivity of ICPs seems difficult compared to MOSs. Thus, most reports have been on heterogeneous MOS/ICP junctions, while the development of pure polymeric heterojunctions is extremely rare.[26,27] Furthermore, the hybridization of polymeric and inorganic semiconductors may reduce the regularity and crystallinity of nanofibers, limiting ICT. In contrast, studies on pure organic nanofibril heterojunctions were mainly focused on π-conjugated molecules and oligomers

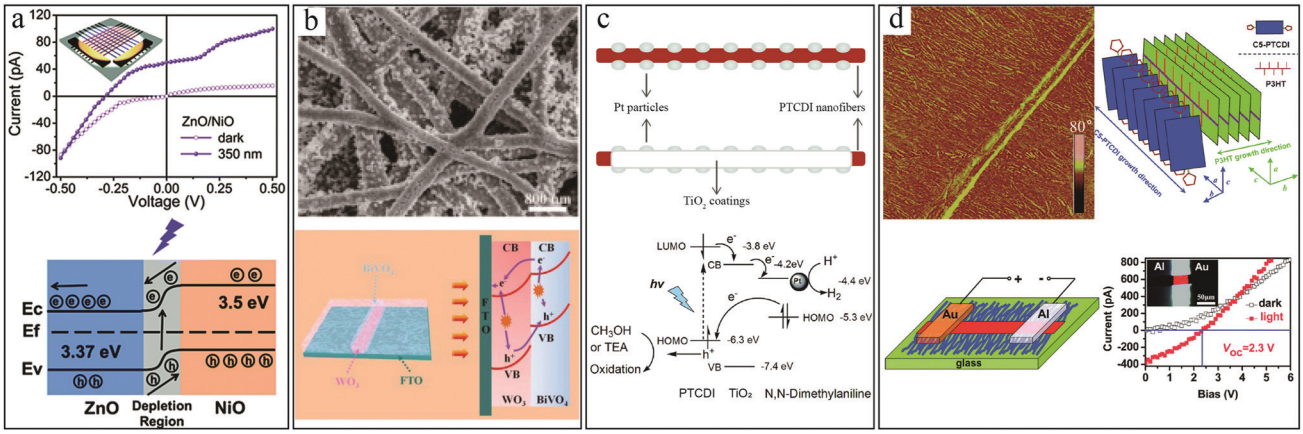

Fig. 1 Schematic illustration of representative optoelectronic systems using nanofibril heterojunctions. (a) Heterojunction array photodetector with orientation distribution of ZnO/NiO nanofibers and their *I*–*V* curves, and the band diagram of ZnO/NiO heterojunctions under UV illumination at 0 V bias. Reproduced with permission from ref. 34, copyright 2019 Royal Society of Chemistry. (b) SEM image of WO_3/$BiVO_4$ nanofibril heterojunctions on FTO as a photoanode for photoelectrocatalytic water-splitting, and the proposed ICT mechanism. Reproduced with permission from ref. 35, copyright 2018 Elsevier B.V. (c) Schematic diagram of Pt/PTCDI and Pt/TiO_2/PTCDI nanofibril heterojunctions for photocatalytic water-splitting H_2 evolution and the proposed mechanism for the latter. Reproduced with permission from ref. 37, copyright 2014 Royal Society of Chemistry. (d) Topographical image and schematic illustration of the intermolecular orientation in a shish kebab-like C5-PTCDI/P3HT nanofibril heterojunction for OPVs and the device architecture and the corresponding *I*–*V* characteristics measured in the dark and under simulated AM1.5G light illumination (the inset shows an optical microscopy image of the device).[39] Reproduced with permission from ref. 39, copyright 2013 Royal Society of Chemistry.

via solution synthesis.[26,27] In the past decade, a series of promising nanofibril heterojunction structures based on PDI assemblies *via* π–π stacking or noncovalent donor/acceptor (D/A) interaction earned the interest of our group.[21,42] Self-assembled PDI nanofibers exhibit excellent crystallinity, fluorescence adjustment, and photoconductive features, making them attractive candidates in organic electronics. In 2014, an inorganic/organic heterojunction based on TiO_2 coated with PDI nanofibers was constructed by us for visible-light-driven photocatalytic H_2 evolution (Fig. 1c).[37,38] Also, we developed a shish kebab-like p/n heterojunction composed of single crystalline C5-PDI nanobelts as a central trunk serving mainly as the primary visible-light absorber providing excited electrons, and highly regioregular poly(3-hexylthiophene) (P3HT) nanofibers as branches acting as an electron acceptor and 1D conductor (Fig. 1d).[39]

As an example of another type of heterojunction, p–p CuO–NiO/C nanofibers for multifunctional imaging and biosensing of target cancer cells in whole blood *via* pressure and fluorescence dual signals were reported.[40] A metal/n-MOS heterojunction Cu/ZnO was used to diagnose malaria *via* protein biosensing.[41]

Despite tremendous research efforts on PVs and FETs, fewer reviews have been dedicated to the topic on tuning ICT processes and mechanisms in CRSs by judiciously tailoring nanofibril heterojunctions in terms of their components, morphologies and architectures. The following section will cover and highlight the latest advances of this hot and burgeoning research field.

3. Tunable nanofibril heterojunctions for CRSs

CRSs for gas detection are one critical branch of the applications of nanofibril heterojunctions. Their performances are associated with parameters including (a) response, usually defined as R_{gas}/R_{air}, representing the variation ratio of resistance or conductance in the presence of gaseous analytes to that in air at the initial level; (b) response or recovery time, defined as the time to reach 90% of its equilibrium value after exposure to the analyte or a decrease to 10% of its original state after removing the analyte; (c) sensitivity, defined as the response *versus* concentration of the targeted analyte obtained from the slope of a calibration curve; (d) selectivity, defined as the response disparity between the targeted analyte and interfering gases (also referred to as cross-reactivity); (e) lowest detection limit (LDL), with respect to the lowest detectable concentration of an analyte; (f) reversibility, the extent to which the conductance signal returns to its initial state after exposure to the analyte; (g) stability and drift, determined by unchanged behavior over the lifetime of the device; and (h) hysteresis, freedom from stimuli-dependent measurements over time or in devices.[4,18,23] In cases (a)–(g), apart from working temperatures and bulk-phase construction, all are significantly governed by semiconductors and components like catalysts, in conjunction with ICT processes among the adsorbed molecules, contact surfaces, and hybrid interfaces.

In Fig. 2, we present the commonly reported constructions of heterojunction nanofibers and involved individual components. Nevertheless, CRSs based on single type nanofibers have relative advantages and distinct disadvantages. In general, the fabrication of MOS nanofibers requires much higher power consumption, and operation of MOS nanofibril sensors requires high temperatures, thus also consuming high power. MOS sensors can be poisoned by sulfur or weak acids, and often suffer from limited sensing ranges depending on high working temperatures. The versatile structures with functionalities of ICP nanofibers and fibril molecular nanoassemblies and intrinsic porous features with abundant defect sites of

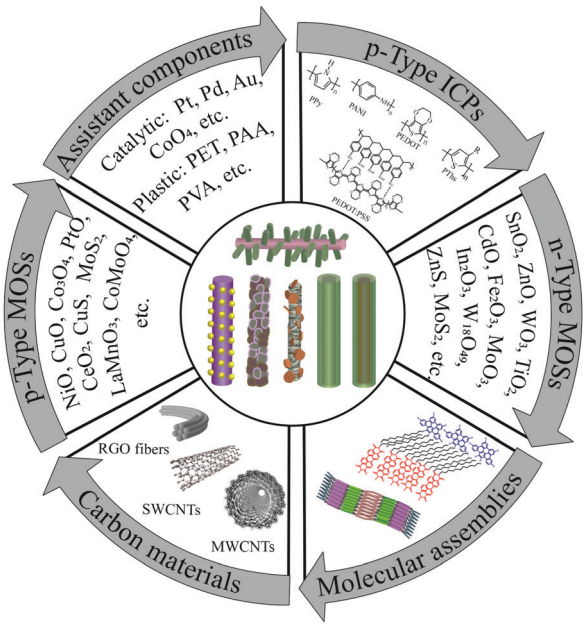

Fig. 2 Typical structures of heterojunction nanofibers and related semiconducting or assistant components mostly reported in the past decade.

CNTs all have large adsorptive capacity and room temperature (r.t.) sensitivity and selectivity toward analytes. CNTs all require difficult synthesis methods, exhibit limited dispersibility and selectivity and thus often need functionalization or oligomer/polymer modification. Also since the inner tubes in MWCNTs inhibit their exposure to analytes, most studies on CNT-based CRSs are on SWCNTs.[14,15]

Specially, assembled nanofibers of PTCDIs benefit high 1D crystallinity, easy solution fabrication, extremely low LDL for vapor sensing, though the rigid molecular configuration may cause limited mechanical stability of the nanofibril materials.[23] In contrast, nanofibers of ICPs keep their high elasticity and facile morphology adjustment intrinsic to polymer materials. These polymers are controllable in conductivity, flexible for device fabrication, and widely sensitive to many VOCs at room temperature. Merely, they show possible overloading by certain analytes, limited sensor lives, and structural degradation (especially PANI and PPy).

The development of nanofibril heterojunctions containing multiple semiconductors occupies a major research topic in this field. Additionally, the contradictory effect of some structural properties on device performances should be quite considered and tackled. For instance, larger surface area and stronger analyte–sensor interaction could offer faster response, higher sensitivity, and a lower LDL but could possibly degrade selectivity and recovery. In the following sections, our main focus is on inorganic/inorganic, inorganic/organic, and organic/organic nanofibril heterojunctions fabricated from MOSs, SWCNTs, ICPs, PTCDIs and other active materials. Since the basic working principle behind pure MOS sensors has been elucidated in previous reviews,[24,25] the focus was on tunable ICT natures through aided actions and elaborate configurations in terms of the latest advances. Most detection results towards target gases with regard to previously used nanofibril heterojunctions are listed in Table 1 for comparison.

3.1 Inorganic/inorganic nanofibril heterojunctions

3.1.1 Basic participants and sensing mechanisms. In this section, two types of nanofibril heterojunctions have been introduced based on MOS nanofibers coated with nanoparticles or nanofibers of MOSs or metals. Numerous MOSs have been explored and can be divided into transition and non-transition categories. The former category, including NiO, TiO_2 and MoS_2, shows good catalytic functions, while the latter, with ZnO, CuO and SnO_2 as representatives, exhibits good conductivity and sensitivity which are better for sensor use. Since the sensing ability and ICT properties largely depend on their semiconductor natures, much more commonly, MOSs are classified as n- or p-type in view of the majority charge carriers, *i.e.*, negatively charged electrons or positively charged holes, respectively. The reported n-type MOSs mainly include SnO_2, ZnO, WO_3, α-Fe_2O_3, MoO_3, TiO_2, In_2O_3, CdO, and $W_{18}O_{49}$, and metal chalcogenides ZnS and MoS_2, while p-type MOSs include NiO, CuO, Co_3O_4, PtO, CeO_2, $LaMnO_3$, $CoMoO_4$, CuS, and MoS_2. It should be mentioned that the electronic energy states (work functions, band gap, electronic affinity, *etc.*) of MOSs highly depend on their types, element components, crystallinity, and fabrication methods; thus, there are great or small discrepancies between different compounds, and even sometimes the n- or p-type is not absolute for one kind of MOS (*e.g.*, MoS_2).[24–26]

When exposed to a reducing gas (H_2, H_2S, CO, NH_3, CH_4, ethanol, acetone, *etc.*), a decrease or an increase of the resistance in relation to the interface barrier will be measured for n-type or p-type MOSs, respectively, whereas the effect is reversed for oxidizing gas species (NO_x, CO_2, SO_2, *etc.*). To some extent, n-type MOSs are selected as sensing skeletons due to their superior ambient stability and high response compatibility to devices, but p-type MOSs have better catalytic ability and oxygen adsorption capacity, taking Co_3O_4 as an outstanding representative.[24,43] It should be clarified that the comprehensive feature (n-type or p-type) together with the sensing behavior of certain nanofibril heterojunction sensors depends on the mixing ratio between dissimilar MOSs especially the mixed-grain composite with abundant homo-/hetero-junctions (Fig. 3).[43,44] More complicated, besides the type and ratio, shape and size, inter-phase interaction, surface and interfacial energy, assisting actions like catalytic activity and chemical reactivity, and outer parameters like bulk porosity, gas concentration, and humidity all need attentive modulation to accomplish great detection effects.

The optimization of operating temperatures is also crucial. The response and recovery processes in connection with gas adsorption/desorption are both temperature-dependent. Different interfacial adsorption ways between analytes and sensors, *i.e.*, physical or chemical contact, provide conflicting results.[23] Physisorption through van der Waals forces and other weak, non-specific interactions often leads to low sensitivity and selectivity in sensor performance, though the weak surface

Table 1 Comparison of detection performances towards target gases *via* CRSs based on representative nanofibril heterojunctions mentioned in this paper

Structure	Morphology	Targeted analyte	LDL (ppm)	Response (R_{gas}/R_{air})	Response/ Recovery time (s)	Operating temperature (°C)	Ref.
n/p SnO_2/Co_3O_4	Mixed-grain nanofibers	10 ppm C_6H_6	—	20	10.25	350	43
		1 ppm C_6H_6	—	18.7	13.58		
n/n SnO_2/ZnO	Nanoparticle coated nanowires	10 ppm *n*-butylamine	1	7.3	40/80	240	54
n–n ZnO–SnO_2	Mixed-grain nanofibers	0.1 ppm H_2	0.03	78	74/289	350	57
n/n α-Fe_2O_3/SnO_2	Nanoparticle coated nanowires	100 ppm ethanol	10	22.46	20	300	53
p–n Pd@Co_3O_4–ZnO	Blended nanofibers	200 ppm ethanol	1	59	6/12	240	58
p–n Co_3O_4/α-Fe_2O_3	Core–shell nanofibers	50 ppm acetone	1	11.7	2/20	240	61
p–n NiO–WO_3	Random 1D-1D nanorods	10 ppm H_2S	0.2	230	270/7200	r.t.	44
p–p RGO/CuO	Nanosheet loaded nanofibers	10 ppm H_2S	1	11.7	~380/~100	300	55
p–n NiO–ZnO	Mixed-grain nanofibers	10 ppm H_2	0.1	~60	~50/~90	200	45
n–n SnO_2–ZnO	Mixed-grain nanofibers	5 ppm H_2	0.05	91	~25/~30	300	62
p–n CuO/ZnO	Nanoparticle coated nanoclusters	80 ppm NO_2	10	~13	~125	200	64
p/n $LaMnO_3/SnO_2$	Nanoparticle coated nanofibers	100 ppm ethanol	10	20	6/34	260	65
p–n $La_{0.7}Sr_{0.3}FeO_3/SnO_2$	Nanoparticle coated nanofibers	1 ppm ethanol	0.1	28	15	300	72
p–n Co_3O_4@TiO_2	Coaxial core@shell nanorods	100 ppm ethanol	—	40	1.4/7.2	260	46
n–p $W_{18}O_{49}$@CuO	Coaxial core@shell nanorods	1 ppm NO_2	0.1	7.3	~250	50	50
n–n α-MoO_3@TiO_2	Core@shell nanorods	10 ppm ethanol	10	4.8	40	180	66
p–n MoS_2–TiO_2	2D/1D nanofibers	100 ppm ethanol	50	14.2	~30	150	49
n–n ZnO@In_2O_3	Core@shell nanofibers	100 ppm ethanol	5	31.87	3.7/52	225	48
p–n $CoMoO_4/MoO_3$	Nanoparticles coated nanobelts	100 or 10 ppm TMA	5	105 or 25.3	10	220	51
p–n MoS_2/SnO_2	2D/1D nanofibers	100 ppm TEA	5	24.9	~400/600	230	52
n–p NiO/ZnO	Branch-like nanofibers	50 ppm ethanol	7	6.7	Very fast[a]	400	47
		100 ppm acetone	11	10			
p–n Bi_2WO_6/TiO_2	2D/1D nanofibers	100 ppm ethanol	0.5	21.6	15/10.1	r.t.	68
p–n $NiCo_2O_4$@SnO_2	Core–shell nanotubes	100 ppm ethanol	5	8.87	~115/~145	160	69
n–p WO_3–RGO	Thorn-bush nanofibers	5 ppm NO_2	1	9.67	180/432	100	70
p–n PANI/WS_2	1D/2D nanofibers	100 or 200 ppm NH_3	50	~21 or 81	260/790	22	74
p-PANI/p-CuO-n-TiO_2-SiO_2	Nanofiber membrane	100 ppm NH_3	0.4	45.67	~600	r.t.	75
p–n PPy/ZnO	Nanoparticle covered nanofibers	30 ppm NH_3	10	34 ± 2	~50 to 1150	r.t.	73
p–n PPy/SnO				25 ± 2			
p–n PPy@SnO_2	Tube-in-tube nanofibers	1 ppm DMMP	50	~7	1/30	r.t.	76
Tg-Car/SWCNTs	Polymer combined nanotubes	NT, TNT, DNT	ppb	—	$\times 10^1$	r.t.	78
P3AT/SWCNTs		Alkanes	ppm	—		r.t.	79
P3CT/SWCNTs		NMPEA	4 ppb	—		r.t.	80
HFIP-PEDOT/SWCNTs	Polymer combined nanotubes	5 ppm DMMP	6.5	~1.5	—	r.t.	82
D/A ACTC/PTCDI-DD	Heterojunction nanoassemblies	Saturated alkanes	1% sat.	6–15	~2–11	r.t.	97
D/A FTS/DTC	Heterojunction nanoassemblies	8 ppm or 80 ppb NH_3	380	~4	~0.6 or 2.8	r.t.	92

[a] Note. Limited by the filling time (*ca.* 240 s–300 s) to fill the test chamber.

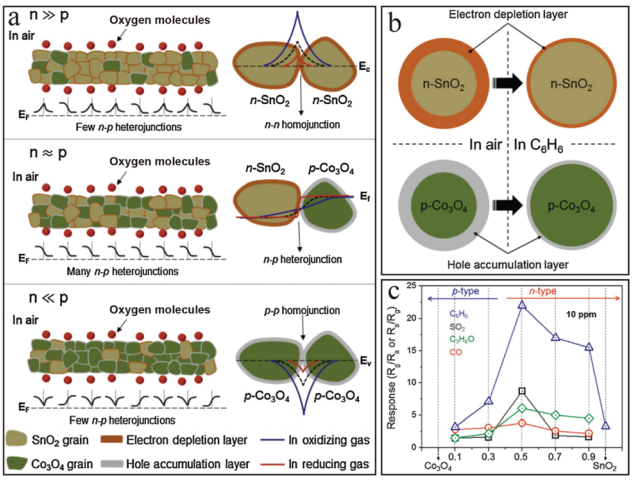

Fig. 3 Illustration of composition-dependent n–p type $xSnO_2$–$(1-x)Co_3O_4$ nanofibril heterojunctions with mixed-grain morphologies in CRSs. (a) Schematic diagram of junctions with selected compositions. (b) Cross-sectional views of the sensing mechanisms of pristine SnO_2 and Co_3O_4 in the presence of air or C_6H_6. (c) Comparison between the responses of sensors to 10 ppm gases at 350 °C. Reproduced with permission from ref. 43, copyright 2017 Elsevier B.V.

adsorption (resulting in easy desorption) helps achieve fast and even complete sensor recovery. In contrast, chemisorption based on stronger chemical bonds often results in high sensitivity and selectivity but slow recovery. For almost all MOSs, sophisticated processability and high operating temperatures (*ca.* 250–450 °C) are necessary to realize useful sensitivity because of the changing oxygen stoichiometry and electrical activation of the surface charges, although elevated temperatures could have adverse effects on sensor stability and lifetimes, as well as increasing power consumption.

Back to the initial sensing mechanisms maintained by ICT processes, they rely on the formation of interfacial depletion layers (also defined as the Debye area) originating from the physicochemical adsorption of O_2 molecules with a large electronegativity of 0.43 eV on pure MOSs' surfaces at increased temperatures.[13] In general, the following extraction of electrons from the conduction band of n-type MOSs forms oxygen ions (molecular O_2^-, and atomic O^- or O^{2-}) at elevated temperature (eqn (1)–(4)).[45] As a result, an electron depletion layer appears at the surface along with increasing resistance owing to the decreasing electron concentration.[24] If the sensor is exposed to reducing gas molecules, their reactions (eqn (6)–(10)) with these surface oxygen species will provide trapped electrons back to the conduction band of n-type MOSs, resulting in the thinning of the depletion layer and, as a result, decreased resistance as a detection signal.[8,43–48] In contrast, for p-type MOSs, a hole accumulation layer is formed due to the same adsorbed oxygen reaction, leading to a decreased resistance, which can be changed back *via* the thickening of the hole accumulation layer through the recombination of the holes in the VB with released electrons from the reducing gas (eqn (5)).[13,25,49] In contrast, the exposure to oxidizing gases offers opposite conductance signal response (eqn (11)–(15)).[50–52] Furthermore, a shift in the equilibrium states of the surface oxygen reaction of MOSs with the contact of the targeted gas analyte occurs at an optimum working temperature.[45] Physically, higher temperature promotes the conversion of O_2^- (<150 °C) to O^- (stable at 150–400 °C) or O^{2-} (stable at >400 °C).[44] Thus in most cases, O^- and O^{2-} are concomitant on the surfaces owing to the relatively lower working temperatures of nanofibril heterojunction sensors (150–300 °C) compared with the dominant O^{2-} ion for the above-discussed pure MOS-based sensor.[44,53]

The initial interface oxygen reactions, and recombination of electrons and holes are as follows:

$$O_{2(gas)} \rightarrow O_{2(ads)} \quad (1)$$

$$O_{2(ads)} + e^- \rightarrow O_{2(ads)}^- \quad (2)$$

$$O_{2(ads)}^- + e^- \rightarrow 2O_{(ads)}^- \quad (3)$$

$$O_{(ads)}^- + e^- \rightarrow O_{(ads)}^{2-} \quad (4)$$

$$e^- + h^\circ \leftrightarrow \text{Null} \quad (5)$$

Interface reactions upon exposure to typical reducing gaseous analytes are as follows:

$$C_2H_5OH_{(ads)} + O_{(ads)}^{2-} \rightarrow CH_3CHO_{(g)} \quad (6)$$

$$C_2H_5OH_{(ads)} + 6O_{(ads)}^- \rightarrow 2CO_{2(g)} + 3H_2O_{(g)} + 6e^- \quad (7)$$

$$2H_2S_{(ads)} + 3O_2^- \leftrightarrow 2H_2O_{(g)} + 2SO_{2(g)} + 3e^- \quad (8)$$

$$HCHO_{(g)} + 2O_{(ads)}^- \rightarrow CO_{2(g)} + H_2O_{(g)} + 2e^- \quad (9)$$

$$2NH_{3(g)} + 5O_{(ads)}^- \rightarrow 2NO_{(g)} + 3H_2O_{(g)} + 5e^- \quad (10)$$

Interface reactions upon exposure to typical oxidizing gaseous analytes are defined as follows:

$$NO_{2(g)} + e^- \rightarrow NO_{2(ads)}^- \quad (11)$$

$$NO_{2(ads)} + O_{(ads)}^- + 2e^- \rightarrow NO_{2(g)}^- + 2O_{(ads)}^- \quad (12)$$

$$CO_{2(ads)} \rightarrow CO_{2(g)} \quad (13)$$

$$CO_{(ads)} + O_{(ads)}^- \rightarrow CO_{2(ads)}^- \quad (14)$$

$$CO_{2(ads)}^- + CO_{2(g)} \rightarrow e^- \quad (15)$$

Interfacial reactions induced by a catalysis, metallization, or sulfurization exposure to special gaseous analytes are described by:

$$H_{2(ads)} \rightarrow 2H_{(ads)} \quad (16)$$

$$2H_{(ads)} + O_{(ads)}^- \rightarrow H_2O_{(g)} + e^- \quad (17)$$

$$NiO + H_2S_{(ads)} \rightarrow NiS_{(1-x)} + H_2O_{(g)} \quad (18)$$

$$WO_3 + H_2S_{(ads)} \rightarrow 2WS_{(2-x)} + H_{2(g)} \quad (19)$$

$$CuO + H_2S_{(ads)} \rightarrow CuS + H_2O_{(g)} \quad (20)$$

$$CuS + 3/2O_{2(ads)} \rightarrow CuO + SO_{2(g)} \quad (21)$$

In a heterojunction nanofiber, there is an additional interface between two dissimilar MOSs leading to desirable Fermi level-mediated charge flow from the higher energy states of one

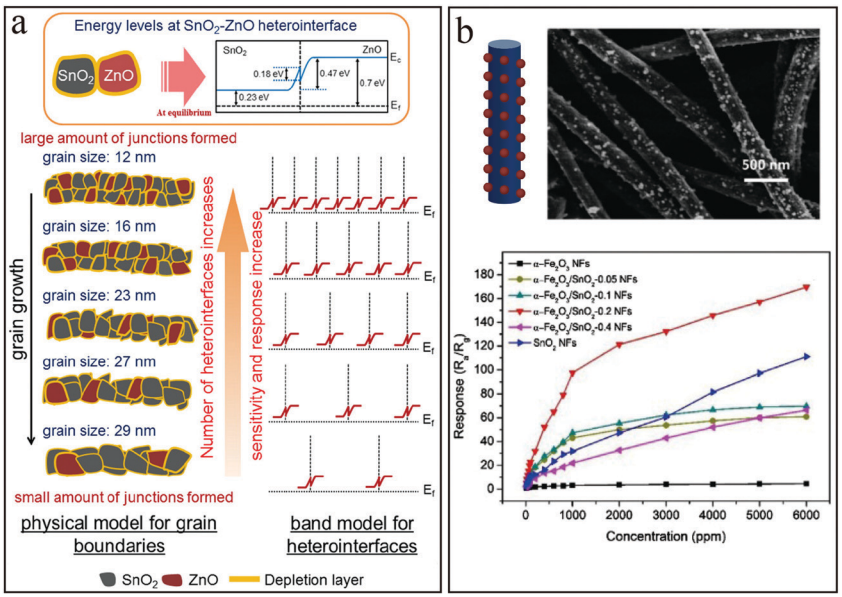

Fig. 4 Illustration of (a) the grain size-control effect of mixed-grain ZnO–SnO_2 nanofibril heterojunctions on H_2-sensing performances. The sensor with the smallest nanograins (*i.e.*, 12 nm) showed the best sensing properties.[57] Reproduced with permission from ref. 57, copyright 2015 Elsevier B.V. (b) Schematic illustration and SEM image of an α-Fe_2O_3/SnO_2(0.2) heterostructure in the form of nanoparticles evenly decorated nanofibers, and responses to different concentrations of ethanol at 300 °C corresponding to varying SnO_2 contents.[53] Adapted and reproduced with permission from ref. 53, copyright 2018 Elsevier B.V.

component to unoccupied lower energy states of another to create a new Debye region at the interface.[24] Such an equilibrating tendency of the Fermi levels across the heterojunction interface to the same energy is driven by work function and energy level differences.[24] Two key parameters relevant to the depletion layer, that is, the width and height, are also positively related to the difference of work functions between two different MOSs to give a direction to select combined components in heterojunctions.[44,54] Within an n–p heterojunction, electrons tend to spontaneously transfer from the n- to p-type component, while the holes will move in the opposite direction to create an interface barrier at the charge depletion layer with the bending of energy levels and thus increase the initial electrical resistance in sharp contrast to individually pure MOSs.[43] Electron–hole recombination at n/p junction interfaces can result in fewer free carriers, making p/p or n/n junctions good candidates for tuning ICT behavior.[24,25] In 2016, n/n type SnO_2/ZnO nanofibers were constructed as effective amine sensors with excellent long-term stability up to three months.[54] Recently, p/p type 0.5 wt% RGO/CuO nanofibers were demonstrated with good selectivity to H_2S gas, benefiting from the intrinsic sensitivity of CuO towards H_2S.[55] But in view of the higher amount of oxygen adsorption in p-type MOSs than that in n-type ones, the research on p/p heterojunction gas-sensing materials is still less.[25,51,55]

Apart from MOSs and gas analytes, the characteristic working temperature corresponding to special gas should be optimized because an efficient oxidation will significantly tune the electron or hole concentration at the surfaces and inner interface of heterojunction nanofibers and subsequently a further enhanced or decreased resistance. Such larger or lower initial resistance means easier signal modulation and thus better sensitivity and remarkably preferable response, as well as low-temperature sensing.[48]

Most distinguishingly, the high sensitivity and rapid response of nanostructured MOSs regardless of morphologies are mainly attributed to the relatively larger depletion layer with an optimal Debye width (δ, typically on the order of 2–100 nm) comparable to the small radius of nanofibers or grain sizes of nanoparticles.[25,43,56] On one hand, it provides a possibility to strongly vary the initial resistance of the heterojunction nanofibers on the basis of δ confinement. On the other hand, it facilitates fast hole and electron diffusion across the junction interfaces which can be depleted by the gas to which they are exposed. In particular, as shown in Fig. 4a, unlike popular core–shell heterojunction structures, the nanograin size control closely to the Debye length and optimum binary content ratio will offer excellent sensing capability to H_2 in the range of 0.1–10 ppm of mixed-grain ZnO–SnO_2 nanofibers with unique long-term stability at 25 °C and a relative humidity of 60% for six months.[57] Furthermore, concentration-dependent (within a range of 10–100 ppm) response to ethanol was demonstrated when adjusting hierarchical α-Fe_2O_3/SnO_2 under optimum nanograin size (Fig. 4b).[53] Theoretically, the height of the depletion region will also be reduced, resulting in an enhanced ICT demonstrated by a decreased resistance. The small dimensions and high aspect area surface can amplify the effects to decrease surface activation energy and enhance charge migration and separation along axial conduction channels.[24]

3.1.2 Tunable ICT *via* assisting catalysis, metallization, or sulfurization. Beyond active semiconductors, enhanced activity can be achieved by controlling the ICT process. Conventionally, catalytic functionalization by attaching metallic nanoparticles

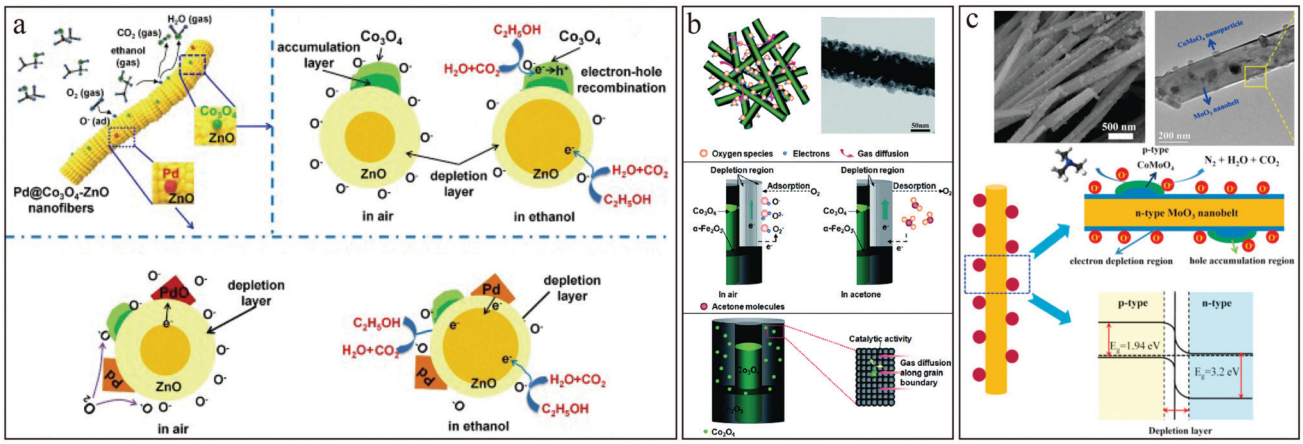

Fig. 5 Schematic of the functional catalytic effect on the tunable interface actions of inorganic nanofibril heterojunctions. (a) Schematic model of Pd@Co_3O_4–ZnO nanofibers upon exposure to air and ethanol gas. Reprinted with permission from ref. 58, copyright 2018 Elsevier Ltd. (b) Schematic diagram of gas diffusion through Co_3O_4/α-Fe_2O_3 nanofibers (inset, TEM image) upon exposure to acetone vapor, and the corresponding conductivity as well as the catalytic action of Co_3O_4. Adapted and reprinted from ref. 61, copyright 2015 Royal Society of Chemistry. (c) FESEM and TEM images of $CoMoO_4$/MoO_3 nanofibers and schematic diagram of possible gas sensing mechanisms. Reprinted with permission from ref. 51, copyright from 2018 Elsevier Ltd.

(*e.g.*, Pt, Pd, Au, Fe) or p-type MOS nanoparticles like Co_3O_4 on MOS nanofibers is an approach to increase the response to targeted gas.[24,43,46,58–60] These enhancements can be attributed to chemical or electronic sensitization. The former corresponds to a decreased concentration of surface oxygen species *via* their possible reactions following catalytic dissociation of chemisorbed molecules, and the latter originates from the strong electrophilic feature of these catalyzers, which may donate electrons to the depletion layers at their interfaces with a MOS, resulting in higher or lower resistance for n-type or p-type MOSs, respecitvely.[8] In this case, small size (<3 nm) and homogeneous, aggregate-free distribution on the surface of the MOS is highly desirable.[8] For example, improved detection of ethanol can be realized through dehydration or dehydrogenation catalytic reactions.[24] As shown in Fig. 5a, the combined electronic and chemical sensitizations provided ternary Pd@Co_3O_4–ZnO heterojunction nanofibers better response toward ethanol at a relatively lower operating temperature (240 °C).[58] At the same working temperature, with catalytic action from the p-type Co_3O_4 with pre-adsorbed oxygen and hollow core–shell Co_3O_4/α-Fe_2O_3 nanofibers presented superior sensing selectivity to acetone with fast response/recovery (Fig. 5b).[61] By comparison, p–n type $CoMoO_4$/MoO_3 with 0D nanoparticles coated onto 1D nanobelts (Fig. 5c) was demonstrated as an effective trimethylamine (TMA) gas sensor with a high response of *ca.* 105 and fast response and recovery within 10 s at 100 ppm concentration at 220 °C. The catalytic activity of $CoMoO_4$ promotes the oxidation of TMA in combination with crystallographic defects from interfacial lattice mismatch, leading to increased ICT efficiency, and increased adsorption of oxygen and TMA species at interfaces (Fig. 5c).[51]

In another example, in view of the catalytic activity of the Fe element and its doping effects on the mesoporous volume, surface area, oxygen adsorption, and charge carrier concentration, Fe-doped In_2O_3 nanofibers showed temperature and composition-dependent gas response and selectivity toward aromatic benzene, *p*-xylene, and toluene, and non-aromatic formaldehyde and ethanol.[60]

Less commonly, an additional electrocatalytic action of In_2O_3 to promote the oxidation of ethanol has been demonstrated in n–n type ZnO@In_2O_3 core@shell nanofibers, which was beneficial to maintaining their outstanding selectivity, higher response and long-term stability for one month towards ethanol vapor compared to pure ZnO nanofibers.[48]

Surface metallization induced by reducing H_2 has been utilized to provide partial transformation from ZnO to metallic Zn at nanograin boundaries in ZnO-involved heterojunction nanofibers, leading to a significantly decreased resistivity, further improving their sensing capability to H_2.[45,57] As a representative, a metallization effect has been introduced into p–n type NiO/ZnO nanofibers to achieve a LDL of 0.1 ppm H_2 at 200 °C. Additionally, there is a catalytic effect of NiO under optimal 0.05 wt% deposition that can dissociate H_2 molecules into H atoms (eqn (16)), which subsequently react with oxygen ions (O^-) adsorbed on the ZnO surface and release electrons to decrease the width of the interfacial electron depletion layer (eqn (17)).[45] Similar semiconductor-to-metallic surface conversion (Fig. 6a) can be observed for n–n type 0.1 wt% SnO_2 loaded ZnO nanofibers which showed a high response (48) to as low as 50 ppb H_2 at 300 °C.[62]

Surface sulfurization by H_2S of MOSs like NiO and WO_3 has been introduced to construct highly selective chemiresistive H_2S sensors.[44,55] As shown in Fig. 6b, at an optimal molar ratio of 3 : 1 (NiO to WO_3), random nanorod networks of NiO–WO_3 showed n-type selectively sensing behavior to H_2S.[44] In addition to the high initial resistance imposed by the p–n junction effect, the sulfurization action upon exposure to H_2S formed quasi-metallic byproducts (NiS in eqn (18), WS_{2-x} in eqn (19)) that can break through the conduction pathway, and the lower dissociation energy of the H_2S realized a lower LDL of 200 ppb

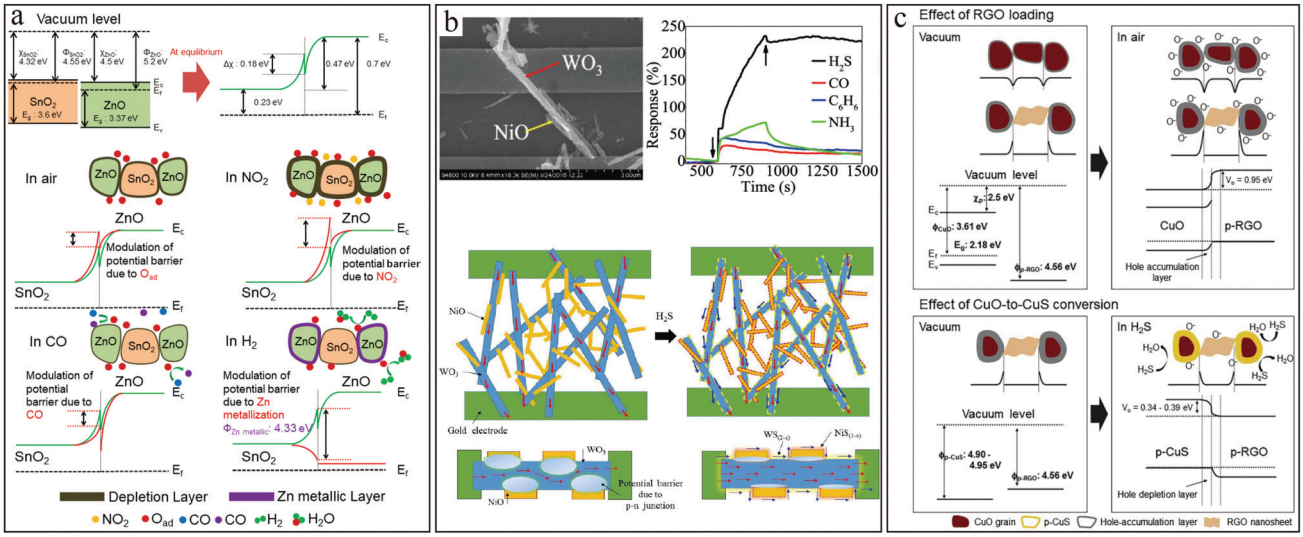

Fig. 6 Schematics of the morphology and mechanisms of inorganic nanofibril heterojunctions involved using assistant models for CRSs. (a) Schematics of the metallization effect in a SnO_2-loaded ZnO nanofiber gas sensor under vacuum, or in air, NO_2, CO or H_2. Reprinted with permission from ref. 62, copyright 2019 Creative Commons Attribution License. (b) FESEM image of NiO–WO_3 (molar ratio 3 : 1) nanofibers, dynamic responses of the corresponding sensors against 10 ppm vapors and schematic of the sulfurization effect on the conduction pathway model during exposure to H_2S gas. Reprinted with permission from ref. 44, copyright 2018 American Chemical Society. (c) Changes in energy band structures with potential barriers in nanofibril RGO–CuO heterojunction sensors towards different gases. Reprinted with permission from ref. 55, copyright 2019 Elsevier B.V.

and a higher response (230) to it (10 ppm) than CO, benzene and NH_3 at r.t., but extremely longer response and recovery times (270 s and 7200 s). In contrast, at the same concentration, no response was observed for bare NiO nanowires. In another work, p–p RGO/CuO heterojunction nanofibers, electrospun from an aqueous solution containing 0.5 wt% RGO nanosheets, showed good selectivity but relatively poor response (11.7) towards 10 ppm H_2S at 300 °C.[55] Sulphurization and the conversion of CuO to metallic CuS (eqn (20)) and oxygen-induced recovery (eqn (21)) played critical roles (Fig. 6c). Similar action was also utilized for the selective detection of SO_2. Recently, pure p-type $LaFeO_3$ nanofibers with a hollow morphology has shown good sensitivity, low LDLs (0.5–4 ppm) and moderate response and recovery times (60–360 s and 180–500 s) toward H_2S and SO_2 at 200 and 250 °C.[63] This is because the interaction with SO_2 at surfaces could promote the formation of SO_4^{2-} accompanied by the injection of electrons directly to the CB.

3.1.3 Tunable ICT *via* morphology. As illustrated in Fig. 3, there are unavoidable n–n or p–p type homojunctions arising from pure single MOS nanograins. They will generate potential ICT barriers across crystal grain interfaces, which have to be considered in the design of grain-mixed heterojunction nanofibers.[45,57] In comparison, metal or MOS nanocrystals coated onto MOS nanofibers can form well-defined nanofibril heterojunctions.[53,54] An optimal coverage of nanoparticles on templated nanofibers is necessary to maintain the best performance, implied by the existence of charge depletion layers. The direct deposition of 0D nanoparticles on MOS nanorod-clusters grown vertically on a seed coating has been widely researched. Such heterostructure nanorods can provide rapid gas diffusion within their cluster configurations. The initially increased resistance of a p–n type CuO/ZnO heterojunction sensor after loading spherical CuO with an average diameter of 10 nm on ZnO nanorods with 100 nm average diameter and 2.5 μm average length resulted in a 10-fold enhancement of response and sensitivity to ZnO nanoclusters alone upon exposure to NO_2 (Fig. 7a and b).[64] With small-size nanoparticles being heavily coated onto the MOS nanofibers in a scattered state, the above nanoclusters formed much more abundant heterojunctions. As shown in Fig. 7, SnO_2/ZnO and $LaMnO_3$/SnO_2 nanofibers were taken as n–n and p–n type heterojunction sensors, respectively. Distinct from the metallization effect in ZnO–SnO_2 nanofibers on H_2 detection,[57] the higher adsorption energy of ZnO contributed to an effective detection of *n*-butylamine *via* SnO_2/ZnO nanofibers (Fig. 7c and d), but the recovery was twice as slow as the response.[54] With a molar ratio of 3/7, $LaMnO_3$/SnO_2 exhibited the largest BET surface area of 33.5 $m^2\ g^{-1}$ and maximum initial resistance, an improved response to ethanol gas arising from the depletion of ICT-induced interface barrier layers (Fig. 7e and f).[65] The catalytic action of perovskite oxide $LaMnO_3$ played a certain role too, whereas highly conductive nanofibers with higher redox activity were almost irresponsive to the tested gases.

Nanofibril heterojunctions with core@shell morphologies are demonstrated as well-ordered architectures providing largely uniform interfaces resulting in built-in electric fields and good ICT across the electron depletion or hole accumulation layers.[48] Usually, the thicknesses of the shells were limited to several to tens of nanometers containing nanocrystals with diameters of several nanometers to realize their optimum effect with core dimensions and Debye length in the heterojunctioned interface. In one instance, coaxial Co_3O_4@TiO_2 nanofibers with a p–n type heterojunction (Fig. 8a and b) displayed a high response of 40 towards 100 ppm ethanol gas with a

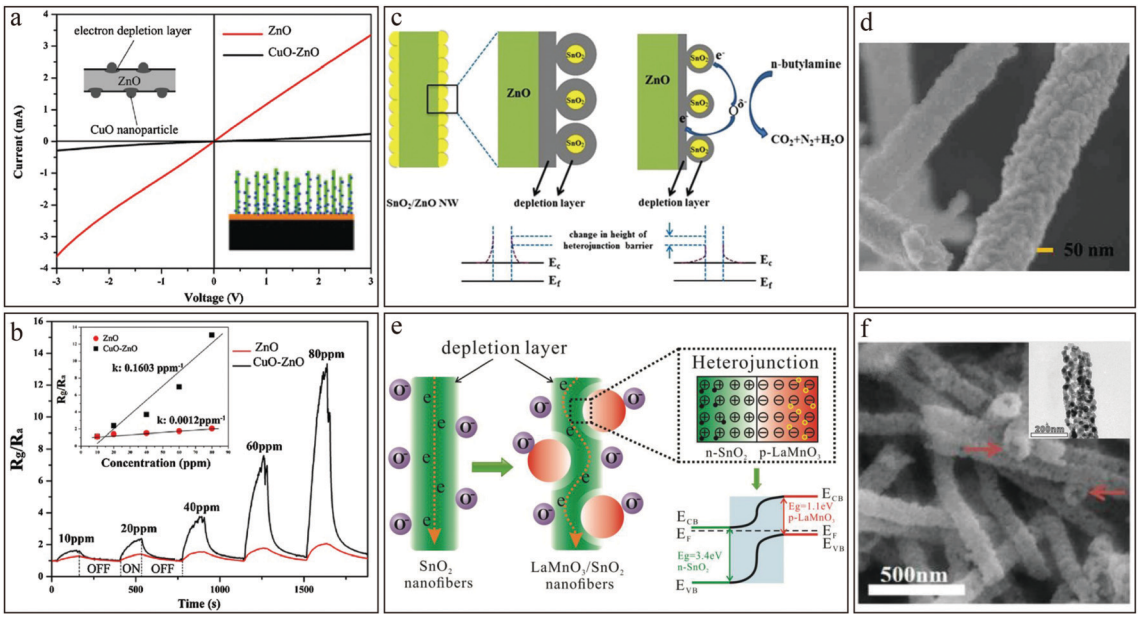

Fig. 7 Illustration of an inorganic nanofibril heterojunction in CRSs in the form of MOS nanoparticle coated MOS nanofibers. (a) Schematic illustration of CuO/ZnO nanoclusters and the *I*–*V* characteristics in N_2 at 200 °C, and (b) the response and sensitivity (inset) for various NO_2 concentrations at 200 °C. Adapted and reproduced with permission from ref. 64, copyright 2013 Wiley-VCH. (c) Schematics of the gas sensing mechanisms of a heterostructure sensor based on SnO_2/ZnO nanofibers and their SEM image (d). Reproduced with permission from ref. 54, copyright 2016 Nature. (e) Schematic illustration of the gas-sensing mechanism for $LaMnO_3/SnO_2$ nanofibers and their FESEM and TEM (inset) images (f) when SnO_2 with molar ratio of 0.3 in the composite. Adapted and reproduced from ref. 65, copyright 2018 Springer.

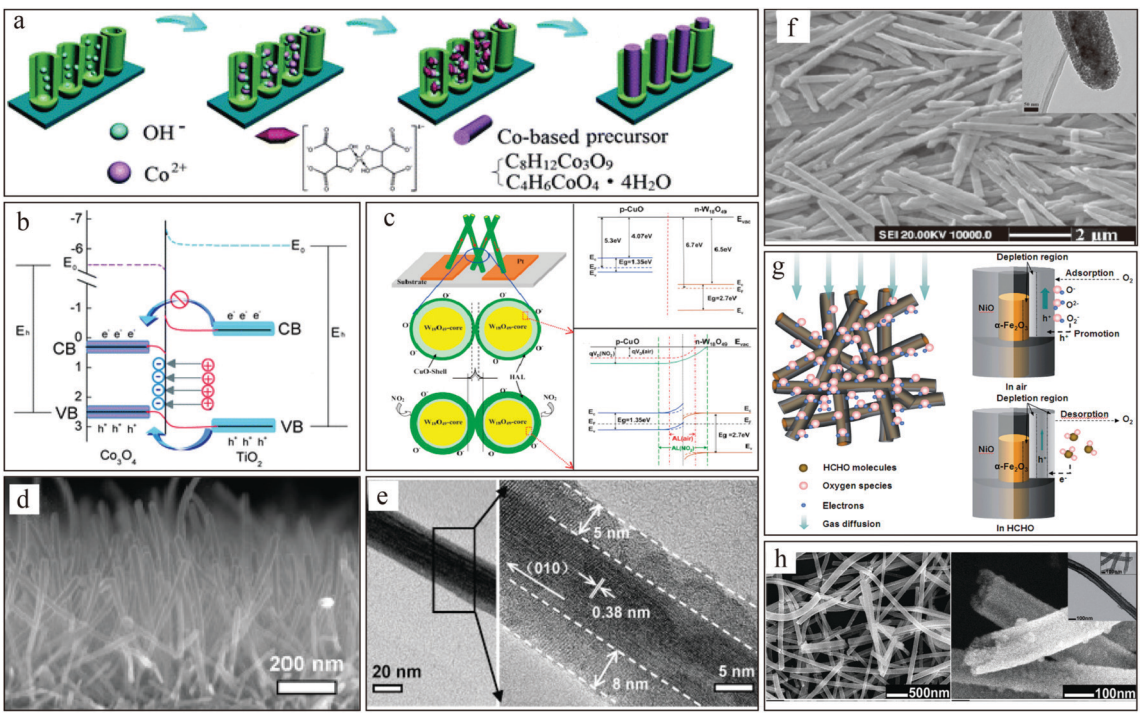

Fig. 8 Illustration of an inorganic nanofibril heterojunction with core@shell morphologies in CRSs. (a) Schematic of the formation of nano-coaxial Co_3O_4@TiO_2 and (b) ICT diagram within the heterojunction. Reproduced with permission from ref. 46, copyright 2013 Royal Society of Chemistry. (c) Schematic illustration of the NO_2-sensing mechanism and energy band diagrams of $W_{18}O_{49}$@CuO aligned arrays and their SEM (d), and low and high resolution TEM images (e) from cross-sectional views. Reproduced with permission from ref. 50, copyright 2016 Elsevier B.V. (f) SEM image of α-MoO_3@TiO_2 nanorods treated in H_2 and air, and HRTEM image (inset) obtained when the concentration of the precursor $Ti(SO_4)_2$ aqueous solution was 0.1 mol L^{-1}, which was annealed under H_2/Ar flow and subsequently in an ambient atmosphere.[66] Adapted and reproduced with permission from ref. 66, copyright 2017 Elsevier Ltd and Techna Group S.R.L. (g) Schematic diagram of gas diffusion through hollow α-Fe_2O_3@NiO nanofibers, and ICT processes in air and HCHO, and (h) low- and high-magnification SEM and high-magnification TEM (inset) images. Adapted and reproduced with permission from ref. 67, copyright 2015 Royal Society of Chemistry.

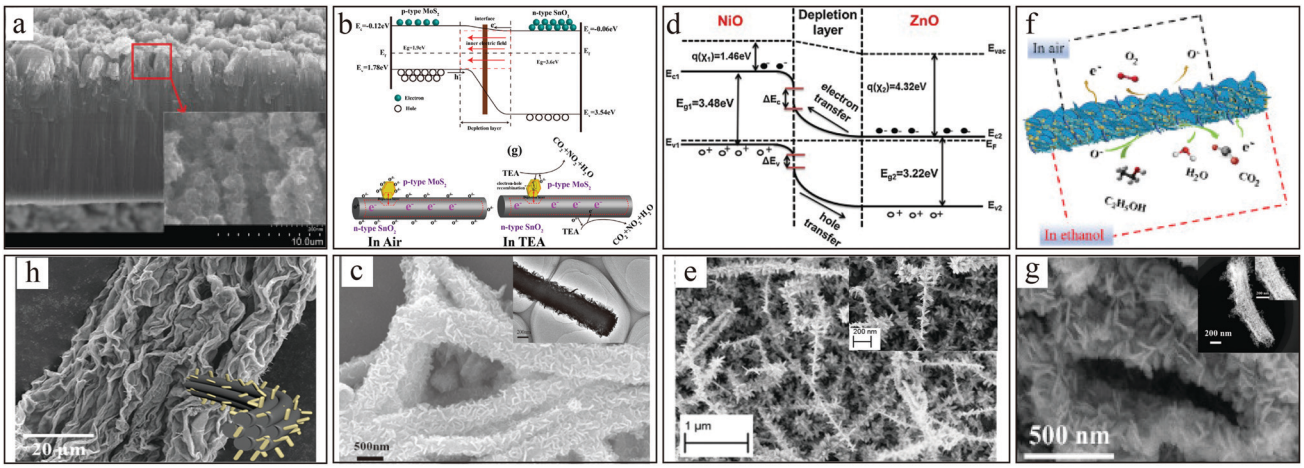

Fig. 9 Illustration of inorganic nanofibril heterojunctions in CRSs in the form of 2D/1D morphologies: (a) SEM cross-sectional images of MoS_2/TiO_2. Reproduced with permission from ref. 49, copyright 2016 Elsevier B.V. (b) Schematic illustration of the energy band of MoS_2/SnO_2 and the sensor model in air and TEA vapor, and (c) SEM and TEM (inset) images. Reproduced with permission from ref. 52, copyright 2018 American Chemical Society. (d) Schematic ICT mechanism and (e) SEM images of NiO/ZnO heterostructures fabricated at 380 °C. Reproduced with permission from ref. 47, copyright 2018 Elsevier B.V. (f) Schematic diagram of $NiCo_2O_4$@SnO_2 nanotubes upon exposure to air and ethanol and (g) SEM and HAADF-STEM (inset) images. Adapted and reproduced with permission from ref. 69, copyright 2019 Elsevier B.V. (h) SEM image and schematic of porous WO_3/RGO nanofibers. Reproduced with permission from ref. 70, copyright 2019 American Chemical Society.

remarkably short response/recovery time of 1.4 s/7.2 s at 260 °C. The catalytic action of Co_3O_4 and its high affinity to chemisorbed oxygen produced were responsible for this high level of performance.[46] Notably, sensors based on highly aligned arrays of $W_{18}O_{49}$@CuO with core@shell nanorods (Fig. 8c) responded well to 0.1–1 ppm NO_2 at 50–200 °C, arising from the formation of n–p type heterojunctions and good vapor diffusion among the nanorod arrays (Fig. 8d and e).[50] The benefits of a uniform core@shell morphology have also been shown for the random stack configuration of nanofibers with large aspect ratios. As shown in Fig. 8f and Table 1, n–n type α-MoO_3@TiO_2 nanorods showed improved ethanol sensing in favor of the highly crystalline shell with an optimal thickness of 30 nm on the uniform homogeneity and smooth surface of the core.[66] The synergy of the hollow architecture and catalytic effect of p-type MOSs was introduced into α-Fe_2O_3@NiO nanofibers (BET, 103.1 m^2 g^{-1}), which demonstrated excellent HCHO sensing performances (Fig. 8g and h).[67] In contrast to the core@shell fibers, hollow heterojunctions exhibit large aspect surface area, beneficial to gas diffusion and adsorption/desorption.

Different from ordinary architectures, heterojunctions assembled from 2D nanosheets coated onto 1D nanofibers have to be given special attention because specific surface area is a vital factor that should be taken into account to control the interfacial interaction and subsequent ICT behavior, which provides active sites to absorb oxygen molecules and targeted gas.[25,47,49,54,68] For instance, 2D MoS_2 nanoflakes coated on TiO_2 nanotubes (Fig. 9a) not only form a p–n heterojunction with grain boundaries that provide potential ICT barriers at interfaces, but also double the BET surface area.[49] These aspects were favorable for detecting ethanol gas with increased response about 11 times that of undecorated TiO_2 nanotubes. It's noted that the increased BET surface area is not always the only or decisive factor for enhanced sensing performances. Specifically, MoS_2/SnO_2 from vertically-grown 2D MoS_2 nanosheets on the surfaces of SnO_2 hollow nanofibers was studied as an highly selective sensor towards trimethylamine (TEA) vapor with a maximum response of 106.3 for 200 ppm at 230 °C (about 11 times greater than that of a pure SnO_2 sensor), outstanding reproducibility and favorable long-term stability over two months (Fig. 9b).[52] Although the uniform 2D/1D configuration together with the highly porous structure of such nanofibers (Fig. 9c) lead to a BET surface area of 24.25 m^2 g^{-1}, the value is not significantly larger than that of bare SnO_2 hollow nanofibers. As a consequence, it was the fundamental electron-donating ability of TEA and its strong adsorption onto the fully-exposed Mo ion sites, which showed Lewis-acidic character at high temperature rather than large surface area playing the critical role. Similarly, branch-like heterojunctioned NiO/ZnO nanofiber sensors have shown lower LDLs of 7 ppm for ethanol and 11 ppm for acetone at 400 °C. It is identified that such sensors showed n-type character (Fig. 9d) because of the full coverage of n-type ZnO on the 1D backbone of the NiO nanowires by epitaxial growth on their branches (Fig. 9e).[47] In particular, the combination of core–shell and hierarchical 2D/1D morphologies, a p–n type $NiCo_2O_4$@SnO_2 nanotube-based sensor (Fig. 9f and g) demonstrated good sensitivity to ethanol with a low LDL of *ca.* 5 ppm and long-term stability over one month.[69] Recently, similar architectural design with special morphologies has captured much interest in constructing reliable CRSs by controlling interfacial actions.[69–71] Through uniform decoration of catalytic WO_3 nanorods onto ultraporous RGO nanofibers, n–p type WO_3/RGO nanofibers with wrinkled surface morphology showed improved NO_2 sensing down to as low as 1 ppm at r.t. when they were integrated in watch-type wearable devices.[70] Hierarchical nanostructures of

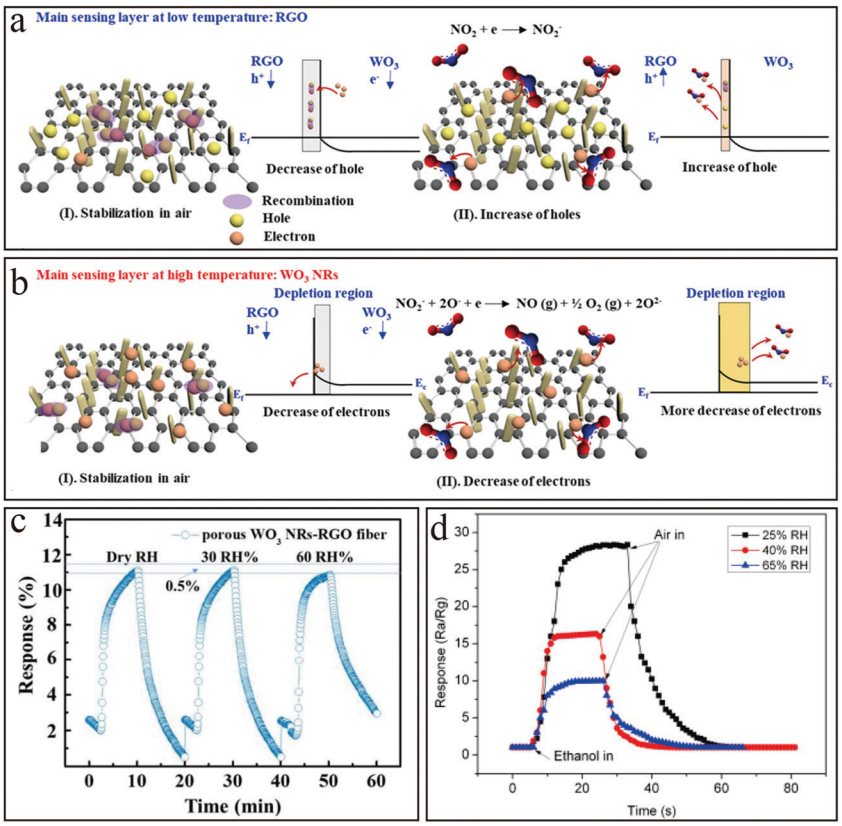

Fig. 10 Illustration of temperature and humidity stability in CRSs. Schematic of the sensing mechanism of porous WO_3–RGO nanofibers at low (a) and high temperatures (b), and dynamic 10 ppm NO_2 sensing response depending on the humidity (c). Reproduced with permission from ref. 70, copyright 2019 American Chemical Society. (d) Response/recovery behavior of $La_{0.7}Sr_{0.3}FeO_3/SnO_2$ nanofibril sensors to 1 ppm ethanol under various humidity conditions.[72] Reproduced with permission from ref. 72, copyright 2013 Elsevier B.V.

homogeneous MOSs with diverse morphologies were also given some attention. For example, a gas sensor based on SnO_2 nanosheets covered with hollow SnO_2 nanofibers showed a higher response (57) and shorter response/recovery times (4.7 s/11.6 s) towards 100 ppm HCHO at 120 °C than pure SnO_2 nanofibers or nanosheets.[71]

3.1.4 Tunable ICT depending on temperature and humidity tolerance. MOS-based nanofibril heterojunctions are usually fabricated *via* methods like mix-electrospinning followed by high-temperature (300–600 °C) calcination or pyrolysis.[48] Appropriately high temperatures could maintain their crystalline phase and produce defect sites in the form of electron-donating oxygen vacancies on the nanofiber surface, providing better adsorption of oxygen species.[43] Nevertheless, the processing conditions have highly complex influences on the structures and morphologies and thus sensing performances, but do not change the basic ICT mechanism. Thus, it is beyond our detailed discussion. Here, we just mention that the relationship between the operating temperature and performance of most sensors is positive within a reasonable temperature range. Taking the above-mentioned WO_3–RGO nanofiber as an ordinary example, with the temperature increasing to optimal 100 °C (Fig. 10a), the physisorption/desorption of NO_2 to p-type RGO as a crucial sensing component was related to its faster response/recovery (180 s/432 s), compared to 425 s/448 s under 200 °C controlled by a chemisorption/desorption mechanism for n-type WO_3 as the main sensing component (Fig. 10b).[70] However, in some cases, it is far from absolute. The optimal operating temperature for the maximum sensitivity of nanofibril MoS_2–TiO_2 sensors to ethanol was determined to be 150 °C when the presence of rich active defects beneficial to vapor adsorption played the predominant role.[49] Correspondingly, the effect of improving conductivity due to the increasing crystallinity of MoS_2 accompanied by reduced surface defects was weak. When the temperature reached 300 °C, the response can increase in part where there was partial transformation of MoS_2 to MoO_3. Further increasing the temperature to 350–400 °C cannot lead to increasing response, where there was a competing balance between the adsorption and desorption of the chemisorbed gases. Nevertheless, it has not been reported that a rough morphology comprised of several layers of amorphous MoS_2 on TiO_2 nanotubes must have a negative influence on sensing performance.

The performances of most of the above-listed CRSs could be hindered by the presence of humidity depending on their working temperature. The easy adsorption of water molecules on the surfaces of sensors can prevent the adsorption of oxygen or target gas molecules.[45] Promisingly, through elaborate component and structure modulation of sensing nanofibers, such an issue can be improved to some degree. Particular humidity stability has been observed for detecting NO_2 gas with the

heterogeneous WO_3–RGO described above (Fig. 10c).[70] In addition to long-term ambient stability up to 90 days, benefiting from the humidity-resistant characteristics of p-type perovskite oxide $La_{0.7}Sr_{0.3}FeO_3$ nanoparticles (with a molar percentage of about 3.7% in the composite), their packing on SnO_2 nanofibers provided high responses to ethanol of 28, 16 and 10 at relative humidity levels (RH%) of 0%, 40% and 65%, respectively (Fig. 10d).[72]

3.2 Inorganic/organic nanofibril heterojunctions

As shown in Table 1, inorganic heterojunction nanofiber-based CRSs often need heaters because of their required high operating temperatures. Over the past decade, significant progress has been made in the exploitation of MOS or SWCNT composites with ICPs under less harsh working conditions. In contrast to inorganic counterparts, organic ICP nanofiber-based sensors had fast response/recovery times at r.t. but are frequently unstable at elevated temperatures. Essentially, such a sensing ability relies on sensitive chemical doping/undoping or electrical ionization processes that modulate conductance across a range of several orders of magnitude arising from the different degrees of chemical protonation towards adsorbed gas and redox reaction. These rather interesting electrical properties can be strengthened by the possibility of tuning their values by means of appropriate structural versatility and tunable morphologies. They have been demonstrated as efficient sensors for monitoring extensive organic and inorganic compounds, especially NH_3, NO_x, VOCs, and even biological species with the assistance of optimal working temperatures.[3,5] Additionally, the strong adsorption and binding of gas molecules among the porous structures of the ICP nanofibers are beneficial to sensor sensitivity.[4] However, irreversibility arising from the difficult desorption and relatively poor selectivity of gaseous molecules compared to MOS-based sensors due to their huge affinity towards various polar gases and VOCs as well as moisture present in the environment are the major issues with ICPs on their own.

Hence, individual features from the components could combine their respective complementary advantages in inorganic/organic hybrids. To some extent, hybrid nanocomposites can monitor a much wider range of gases from H_2 and NH_3 to VOCs, liquefied petroleum gas (LPG), *etc.*[5] In general, weak van der Waals interaction, hydrogen bonding, or covalent bonding can form the heterojunction between organic and inorganic materials. Incorporating ICPs into the MOS nanofibers has been among the most promising approaches to fulfill the need to decrease their operating temperatures to nearly r.t. because charge carriers can actively migrate between MOSs and ICPs, providing higher concentrations of reaction sites and fast charge carrier migration at relatively low temperatures.[4,8] Creating such a hybrid frequently requires optimizing sensitivity and selectivity by tuning the ratios of ICPs to MOSs, as well as their structures, architectures, and morphologies.

Previous reports on ICP-based CRSs focus mainly on PANI and PPy due to their easy large-scale synthesis, excellent processability for forming nanofibers, and high affinity and electronic interaction (*i.e.*, doping) with guest molecules at r.t.[3] For instance, PANI has rather different reversible acid/base doping/undoping processes and protonation–deprotonation reactions unlike other ICPs, quite beneficial to their responding to HCl, NH_3, hydrazine, *etc.*[3] By contrast, PPy has relatively good stability and conductivity that make it attractive, but has been limited in use due to its low sensitivity, slow response, and mostly irreversible adsorption.[5] Meanwhile, polythiophenes (PThs) including PEDOTs as another type of ICP exhibit much favorable structural functionality and variability for tailoring binding affinity and specific selectivity for certain analytes, and higher electrical conductance in a highly doped state that can be considerably modulated by undoping through interaction with electron-accepting analytes, decreasing conductivity.[16]

Moreover, there are two other mechanisms that should be considered for CRSs based on ICPs. First, instead of the redox ICT process, the swelling effect plays a critical role in sensing unreactive gases like alkanes, benzene, toluene, *etc.*, whose detection at r.t. is generally difficult.[3,28] The interaction between absorbed gas molecules and the ICP film can cause swelling of the polymer conformation, which increases spacing and thus breaks some electrically conductive paths.[22,73] Such weak physical interaction is usually reversible with the removal of the analyte, returning eventually to the initial structure. Thus, this mechanism is of particular interest for designing organic semiconductor nanofibril heterojunctions. Second, the adsorbed gas species on the polymer surfaces can be secondary dopants to modulate both the electronic and optical properties of ICPs. These features make the design of multifunctional gas sensors practicable. Likewise, complex mechanisms in line with an increased number of parameters that define the behavior of these composites should be carefully explored.

As shown in Fig. 11a, p–n heterogeneous PANI/WS_2 (w/w, 10%) in the form of WS_2 nanosheets embedded in a film of PANI nanofibers showed a porous network morphology.[74] Apart from the sensitivity to NH_3 gas with *ca.* 20 and 80 at 100 ppm and 200 ppm, respectively, based on the ICT in heterojunction interfaces (Fig. 11b) similar to the above discussed depletion forming mechanism. Additionally, good long-term stability over one month can be obtained at r.t. (Fig. 11c). Furthermore, the sensor was resistant to humidity, although competitive adsorption of H_2O and NH_3 molecules at the active sites on the sensor surfaces still existed when subjected to 60% RH (Fig. 11d).

A higher r.t. response of 45.67 to 100 ppm NH_3 gas than other interfering gases was achieved with a tubular p-PANI/p-CuO–n-TiO_2–SiO_2 nanofibril sensor in the form of a flexible film with the help of blend-electrospun poly(vinylpyrrolidone) (PVP).[75] The initial resistance was related to complex interfacial p–n PANI/TiO_2 and CuO/TiO_2 and p–p PANI/CuO heterojunction features, to some extent, similar to the FET structure having signal amplification function. After exposure to reducing NH_3, the electrons transferred from the PANI, which in turn converted into an undoped state. A decreased density of holes in PANI enlarged the depletion layer at the heterojunction interface. Both processes could result in increased resistance. Also, the widened depletion layers and a similar FET effect arising from different heterojunction interfaces within the same semiconductor layer will further increase the resistance.

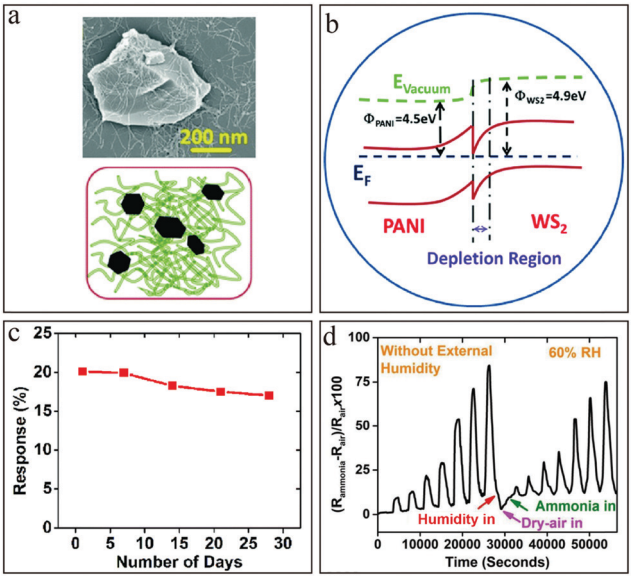

Fig. 11 Illustration of a PANI/WS_2 nanofibril heterojunction in CRSs. (a) FESEM image when WS_2 was 10 wt% and schematic where PANI nanofibers are indicated by a green color, while WS_2 nanosheets are indicated by black hexagonal pieces. (b) Schematic band structures at the interface after interaction. (c) Stability of the sensor. (d) Response in the presence of 60% RH and in the absence of humidity. Adapted and reproduced with permission from ref. 74 copyright 2018 Centre National de la Recherche Scientifique and Royal Society of Chemistry.

Future work should be focused on addressing the issues of PANI, such as an irreversible loss of conductivity in neutral and high pH environments (pH $>$ 5), poor longevity due to natural degradation resulting in a loss of conductivity over time, and relatively slow response time (on the order of hundreds of seconds). For practical use, the response time must be reduced preferably to less than a minute.[5] In this regard, PPy-based nanofibril heterojunctions combined with MOSs seemed promising.

Research on a 1D hollow PPy nanofiber/ZnO nanoparticle-based heterogenous sensor showed that it presented higher selectivity and response (34 $\pm$ 2) than PPy/SnO_2 (25 $\pm$ 2) with the same structures when exposed to 30 ppm NH_3 vapor with a relatively low detection limit of 10 ppm.[73] This sensitivity is ascribed to its higher initial conductivity related to the higher doping state in the presence of p–n heterojunctions and Zn^{2+} cations and thereafter decreased as a result of undoping after exposure to NH_3 and large surface area-to-volume from a special hollow nanotubular morphology (Fig. 12a). The pronouncedly improved linearity demonstrates the consistency of the responses of the PPy/ZnO-based sensor (Fig. 12b). However, the distinct structural deformation and aggregates may hinder its further development. Later, PPy@SnO_2 heterojunctioned nanofibers with a tube-in-tube architecture and a uniform morphology (Fig. 12c and d) were constructed and, at r.t., were highly sensitive (LDL 0.05 ppb), had short response/recovery times of 1 s/30 s and superior selectivity towards dimethyl methylphosphonate (DMMP) vapor, a strong electron-donating toxic gas used as a nerve agent for chemical weapons.[76] The signaling through changing resistance occurred because of the decreased hole concentration *via* electron donation to consume the hole within the thin PPy layer (*ca.* 10 nm). The expanded depletion region across the p–n heterojunction interface due to the electron transfer from SnO_2 to neutralize the holes to maintain the electrical conduction of PPy. Moreover, DMMP molecules had strong hydrogen bonding and high polar interaction with PPy, which can enhance their sensing performance.

Other aspects should also be considered to design inorganic/organic CRSs. For example, no matter what type of heterojunction is used, there are potential barriers in heterogeneous junctions that can interfere with ICT and could adversely affect the sensing performances. The introduction of three-assisted-electrode-electrospinning technology to fabricating heterojunction sensors may be a good method to fabricate uniform, aligned nanofiber arrays on large scales where

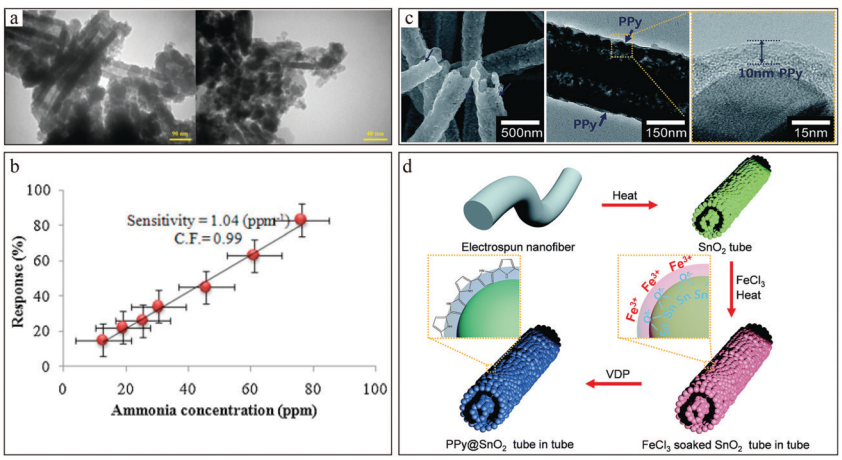

Fig. 12 Illustration of a PPy/MOS nanofibril heterojunction in CRSs. (a) TEM images of hollow PPy/ZnO nanofibers (left) and PPy/SnO_2 (right), and (b) responses of the PPy/ZnO based sensors according to NH_3 concentrations. Reproduced with permission from ref. 73, copyright 2015 Elsevier B.V. (c) FE-SEM, TEM, and high-resolution TEM images of tube-in-tube PPy@SnO_2 heterojunctioned nanofibers, and (d) schematic diagram of the sequential fabrication process. Reproduced with permission from ref. 76, Copyright 2017 Royal Society of Chemistry.

common electrospinning methods seemed ineffective.[34] Metal nanoparticles with small sizes well dispersed on ICPs' nanofiber surfaces could provide another hybrid nanostructure for use in CRSs without a considerable interfacial barrier. PANI nanofiber/Au nanoparticle composites showed promising sensing response to malodor biomarkers H_2S and CH_3SH for breath analysis.[77] Additionally, since the sensing depends on gas absorption and diffusion into the porous nanofibril networks, the morphology of the composite film (smooth, compact, *etc.*) itself can also affect the electrical response to the gaseous analyte and change the sensitivity.[16,78] In addition, since SWCNTs suffer from issues such as poor film quality and large tube–tube junction resistance, hybrid nanostructures combining thin films of SWCNTs with ICPs have also been of great interest in developing high-performance CRSs.[14,78–80] In this case, weak noncovalent modification seems to be a promising choice to vary charge transport behavior while maintaining the original electronic features of SWCNTs, in contrast to robust covalent surface modification.[14,15,81,82] The presence of ICPs, such as robust PThs or polycarbazoles (PCZs) with flexible side-chains, provides the capability to greatly improve the solvent-phase dispersion of SWCNTs, which can be stable for over three years without aggregation and precipitation, and the corresponding sensory performance *via* the swelling effect.[78,79] Theoretically, in the network composites, SWCNTs act the conductive backbones, while ICPs form junctions between adjacent SWCNTs but do not completely cut off charge transport. During exposure to analyte vapor, the ICPs adsorb it, causing swelling of the polymer chains. As a result, the spatial distances of SWCNTs' junctions are enlarged and thus the sensor resistance increases.

In 2014, our group demonstrated that an oligomer of carbazolylethynylene (Tg-Car) can tailor the dispersion and modify the optoelectronic properties of SWCNTs (Fig. 13a).[81] Along with this research, we successively investigated three classes of ICP/SWCNT heterojunctioned nanocomposites *via* solution-phase suspension (Fig. 13b–d).[78,79] Overall, the sensors fabricated by drop-casting these diluted dispersions onto pre-patterned interdigitated electrodes all showed fast and recoverable response to targeted vapors at r.t. Structural swelling-induced charge transfer within porous and continuous membranes was believed to be the core for their discriminately sensing mechanism. Accompanied by an intramolecular donor–acceptor effect and Tg-Car's particular intermolecular affinity to nitroaromatic compounds (Fig. 13b), a significant change in the conductance of the Tg-Car/SWCNTs was measured to differentiate an explosive vapor of 7 ppm of 4-nitrotoluene (NT) from common reagent vapors, with reasonable responses to 0.7 ppb 2,4,6-trinitrotoluene (TNT) and 36 ppb 2,4-dinitrotoluene (DNT).[78] To realize chemiresistive sensing of non-reactive alkane vapors at r.t., three undoped poly(3-alkylthiophenes) (P3ATs) functionalized with linear alkyl side-chains, named poly(3-butylthiophene) (P3BT), poly(3-octylthiophene-2,5-diyl) (P3OT) and poly(3-dodecylthiophene-2,5-diyl) (P3DT), respectively, were combined with SWCNTs (Fig. 13c).[79] In general, a similar length of the linear alkyl chain of an alkane analyte to the length of the side-chain of P3AT resulted in a stronger response. A P3DT/CNT-based sensor showed a detection limit of 342 ppb for *n*-dodecane and 76 ppm for *n*-hexane, and displayed a linear response from 1% to 8% of the saturated concentrations. Meanwhile, a sensor array incorporating all three P3ATs together was able to discriminate different sizes of alkane vapors. When introducing the carboxylic acid group into the end position of the alkyl side-group, an extraordinary sensitivity of poly[3-(6-carboxyhexyl)-thiophene-2,5-diyl] (P3CT)/SWCNTs towards methamphetamine simulant *N*-methylphenethylamine (NMPEA) at concentrations as low as 4 ppb in ambient air was achieved through the acid–base binding interaction between the amine molecules and the

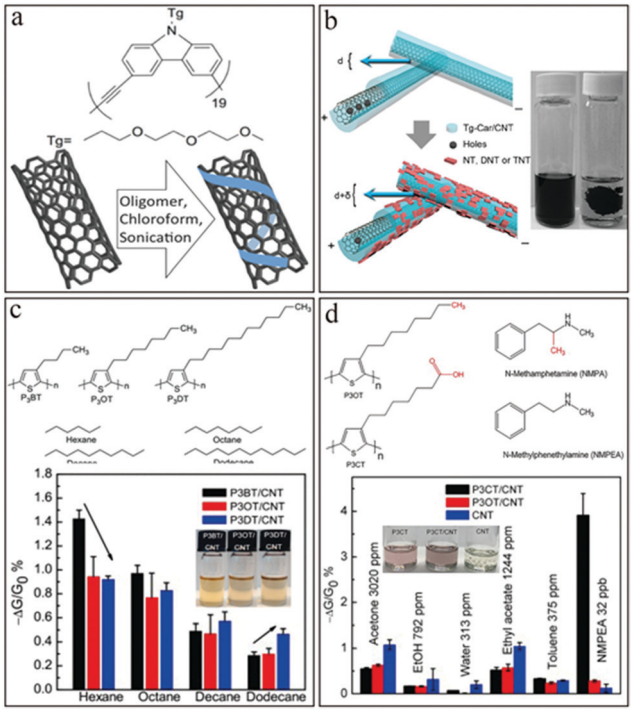

Fig. 13 Illustration of ICP/SWCNT heterojunctioned nanofibers and their sensing properties towards different gaseous analytes. For each test, the analyte exposure time is 20 s and the recovery time is 40 s. (a) Molecular structure of the Tg-Car oligomer and schematic of the functionalization process of Tg-Car/SWCNTs. Reproduced with permission from ref. 81, copyright 2014 Wiley-VCH. (b) Schematic of charge carriers (holes) moving in the SWCNTs and tunneling through the Tg-Car oligomer before and after the exposure to nitroaromatic explosive compounds. And photos of SWCNT suspensions in chloroform with (left vial) and without the Tg-Car oligomer (right vial).[78] Reproduced with permission from ref. 78, copyright 2015 American Chemical Society. (c) Molecular structures of P3ATs and four linear alkane analytes and responses from the three kinds of P3AT/SWCNT-based sensors (three independent sensors for each type) to 8% of the saturated alkane vapors, and photos (inset) of P3AT solutions (7.5 μg mL^{-1}) and P3AT/SWCNT suspensions.[79] Adapted and reproduced with permission from ref. 79, copyright 2017 Elsevier B.V. (d) Molecular structures of polythiophene derivatives (P3OT and P3CT) and NMPA and its analog NMPEA which was used in the vapor sensing tests. Responses of sensors based on P3CT/SWCNTs, P3OT/SWCNTs or non-functionalized SWCNTs towards 20 s vapor exposures of various compounds (1% of saturated vapor) and 32 ppb of NMPEA. Photos (inset) of P3CT (7.5 μg mL^{-1}), P3CT/SWCNTs and SWCNTs in DMSO.[80] Adapted and reproduced with permission from ref. 80, copyright 2018 Elsevier B.V.

polymer (Fig. 13d).[80] Also, its recovery capability was not only better than that of other small amine molecules but also than that of *N*-methamphetamine (NMPA, Fig. 13d), due to the lower surface binding strength from the much higher bulk steric hindrance of NMPEA molecules. Beyond the swelling effect, the decreased sensor conductivity as the detection signal may also be related to the ICT from the electron-donating amine to the uncovered portions of the p-type SWCNTs' surfaces.

Similar PT/SWCNT composites based on the structure design of PTs were also taken by Swager's group. They incorporated hexafluoroisopropanol (HFIP) units on oxidatively polymerized PT (HFIP-PT) and the side-chain of a Kumada catalyst transfer polycondensed PEDOT oligomer (HFIP-PEDOT) to realize their selective detection of DMMP (Fig. 14a).[82,83] The strong H-binding of HFIP to DMMP with a phosphate ester structure can provide great assistance to the swelling- and ICT-induced conductance decreasing mechanism (Fig. 14b). In particular, much more stable HFIP-PEDOT/SWCNTs can show much higher response than those without the HFIP moiety (Fig. 14a), and a lower LDL of 2.7 ppm in N_2 and 6.5 ppm in air with 24% RH than PPy@SnO_2 nanofibers.[76,82]

Nevertheless, in the recent studies, organic–inorganic heterojunction nanofibers still face several issues and challenges. First, control over the crystalline characteristics of nanostructured MOSs still requires high-temperature calcination or other high power-consuming treatments, while their combinations with ICPs are often carried out through hydrothermal, vapor phase deposition, or r.t. processing but with much less regular morphologies.[75] Therefore, the development of heterojunction nanofibers employing ICPs as cores and MOSs as shells was hindered. That is why although the 1D ICP nanofibers with controllable morphologies and sizes have been widely developed in various fields,[36] their promising application for constructing inorganic–organic heterojunctioned nanostructures is still in the early stage. Even for SWCNTs, their combination with nanofibril ICPs is scarcely researched. Second, interfacial mismatch and poor contact between inorganic and organic components and the role of interface junction barriers between SWCNTs and ICPs remain research topics to be sufficiently addressed. Last but not least, the complex components and architectures bring uncertainty to device reliability and the definite sensing mechanism.

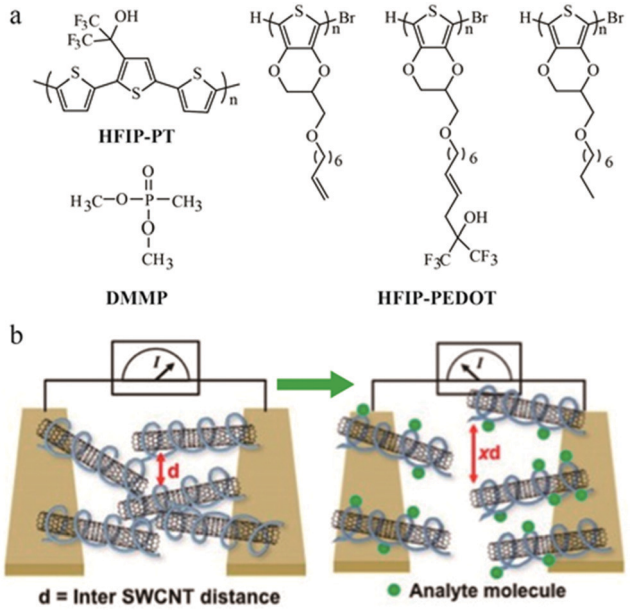

Fig. 14 (a) Molecular structures of HFIP substituted PT (HFIP-PT) or PEDOT (HFIP-PEDOT), and DMMP. (b) Schematic of the DMMP-induced swelling transduction mechanism of HFIP-PEDOT/SWCNTs. Reproduced with permission from ref. 82, copyright 2017 Creative Commons Attribution.

3.3 Organic/organic nanofibril heterojunctions

CRSs utilizing single organic nanofibril heterojunctions can exhibit comparable performances with conventional MOS-based sensors. Combining small molecule organic semiconductors, molecular assemblies, and ICPs with each other can form noncovalently or covalently integrated heterojunctions. However, at present, heterojunction nanofibers combining two or more ICPs have not been extensively researched. Instead, in 2012, homogeneous but multidimensional PPy nanotubes (MPP NTs) were fabricated by vapor deposition polymerization of PPy nanonodules (NDs, Fig. 15a) or nanowires (NWs, Fig. 15b) on a sacrificial 1D tubular PPy nanofiber template built on patterned PDMS substrates.[84] They were highly selective to discriminate NH_3 from 14 analytes in exhaled breath with extremely low LDLs of approximately 10 ppb, and real-time response (less than 1 s) and recovery times (55–60 s; in contrast to 4–5 s for 1 ppm ethanol) (Fig. 15c and d). In contrast to that of MOS/ICP sensors, such performance together with excellent reproducibility and reversibility is required for practical devices. Hence, such a unique architecture like the previously-discussed hierarchical MOS-based heterojunctions and morphological modification will be a promising choice for the future *in situ* polymerization

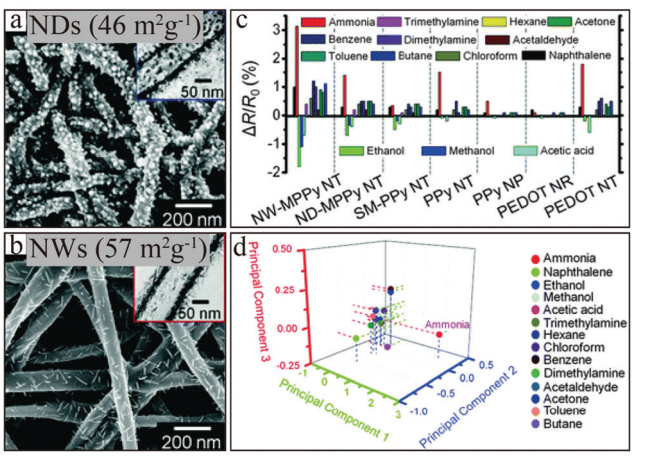

Fig. 15 FE-SEM and HR-TEM (inset) images of multidimensional PPy nanotubes with inlaid NDs (a) and NWs (b). (c) Histogram of sensing performances and (d) principal components analysis plot of the dataset of response intensities inputted from six ICP-based nanomaterials (NW-MPPy NTs, ND-MPPy NTs, SM (smooth layer)-PPy NTs, PPy NTs, PPy NPs (nanoparticles), PEDOT NRs (nanorods), and PEDOT NTs) to 14 analytes (around 10 ppm).[84] Adapted and reproduced with permission from ref. 84, copyright 2012 Royal Society of Chemistry.

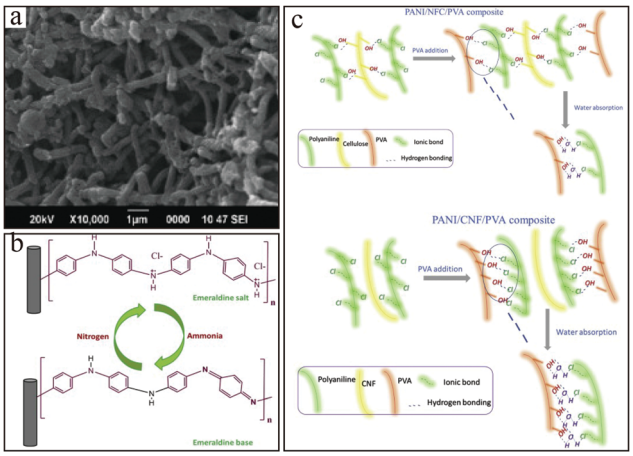

Fig. 16 (a) TEM micrographs of PANI/CNF/PVA nanofibers and (b) the corresponding schematic of the mechanism for NH_3 sensing. (c) Schematics of the mechanisms for the improved humidity sensitivity of PANI/NFC/PVA and PANI/CNF/PVA. Reproduced with permission from ref. 86, copyright 2019 Elsevier B.V.

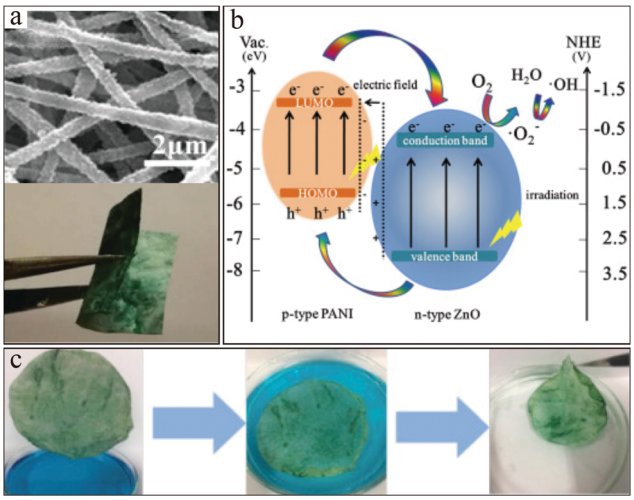

Fig. 17 (a) SEM images of PAN@PANI@ZnO nanofibers prepared using 400 atomic layer deposition (ALD) cycles and photo of the flexible composite under bending. (b) Possible mechanism for the photodegradation of MB dye. (c) Illustration for the possible floating photocatalytic water treatment. Reproduced with permission from ref. 88, copyright 2018 Elsevier B.V.

of one kind of ICP onto nanofibers of another ICP as a template. Certainly, this still encounters challenges, for example, precisely growing regular nanostructures on heterogeneous ICPs' skeletons.

Recently, hybrid nanofibril membranes based on ICPs and non-conductive polymers with the help of electrospinning have been studied as CRSs. By mixing with an insulating polymer like polyvinyl alcohol (PVA), which is usually a necessary auxiliary and consumable material for obtaining electrospun MOS nanofibers, PPy intercalated montmorillonite clay (MMTO) nanoparticles can be converted into interlaced PVA/PPy-MMTO nanofibers (Fig. 16a).[85] Upon exposure to NH_3, their sensing ability may be realized through a decreased resistance signal mainly from conductive PPy chains (Fig. 16b). Utilizing the abundant hydroxyl groups present in PVA and consequently the water-induced polymer chain swelling effect (Fig. 16c), as well as the NH_3 gas-induced protonation/deprotonation effect for PANI, a humidity-resistant NH_3 sensor based on PANI/carbon nanofiber (CNF)/PVA nanofibers was fabricated.[86] In contrast to PANI-PVA, the presence of CNF provided additional porous area for gas diffusion and strengthened the interfacial interaction compared to nano-fibrillated cellulose (NFC), resulting in higher sensitivity and fast response times (41 s to H_2O, 46 s to NH_3) at r.t. in terms of great changes in capacitance/resistance signals. Moreover, electrospun all-insulating polyacrylic acid (PAA)/PVA nanofibers were also used for NH_3 sensors.[87] In this case, the nanofibril materials were coated onto the surfaces of quartz crystal microbalance (QCM) gold electrodes for effective absorption of NH_3.

Such architectures achieved improved processability, mechanical robustness, and thermal stability compared to pure ICP nanofibers but behaved more like composites than heterojunctions. At this point, the immobilization of ICP-based heterojunctions on electrospun common polymer nanofibers warrants further research. For example, immobilization of PANI@ZnO heterojunctions on electrospun polyacrylonitrile (PAN) nanofibers formed multiporous and flexible PAN@PANI@ZnO nanofibers (Fig. 17a).[88] Depending on the improved charge separation of photogenerated electrons and holes among the heterojunction interfaces and 1D migration pathway (Fig. 17b), this film showed excellent photocatalytic degradation activity for methylene blue (MB) dye in water under UV-light illumination (Fig. 17c). This work provides insight into developing flexible CRSs including inert polymers and ICP-based nanofibers with regular heterojunction conformations and good mechanical strength.

Besides electrospinning,[89] another *in situ*, low power-consuming, and templateless strategy, interfacial polymerization (Fig. 18), was developed to fabricate highly crystalline (*i.e.*, defect-free) polymer nanostructures mainly on polyamides, but also later applied to PANI, PPy, and PEDOT nanofibers with confined size distributions and small diameters and/or fibrillar networks as membrane layers.[90,91] The prerequisite is the solubility of aniline, pyrrole and EDOT in special organic solvents being lost upon polymerization. With respect to oxidative polymerization at the liquid/liquid interface, it is commonly governed by either $FeCl_3$ or $(NH_4)_2S_2O_8$ in organic or aqueous solutions to drive mass diffusion and transfer. Due to the additional oxidization reaction, this approach is complex enough to hinder its application but still offers an appealing way to further develop ICP-based heterojunction nanofibers.

In recent years, promising application of interfacial reactions for fabricating heterojunction nanofibers relies on the *in situ* interfacial assembly (Fig. 18) of planar heteroaromatic π-conjugated small molecules, oligomers, or polymers as molecular building blocks.[28,92] Our research indicated that precisely tailorable interfacial interaction due to molecular PTCDIs' π–π stacking can modulate the optical and electronic properties of graphene for vapor detection by opening its bandgap and providing effective photoinduced charge transfer and separation, which

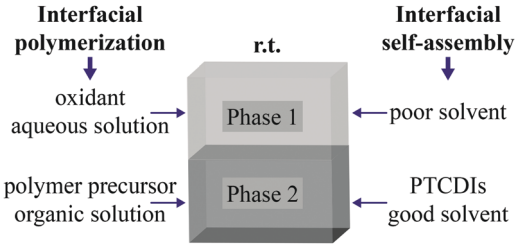

Fig. 18 Schematic diagram of interfacial polymerization for ICP nanofibers and interfacial self-assembly for PTCDI nanofibers.

in turn can be used to construct large-area optoelectronic nanosensors.[93] Noncovalent self-assembly of organic semiconductors without any other additives in the bulk phase opens opportunities for easily constructing well-defined 1D nanofibers with crystallites and surface functionalities. These nanofibers are of special interest in that they exhibit tunable electrical, optical, and stimuli-responsive properties, inspiring excellent applications in CRSs.[28,94]

As with the other types of nanofibers mentioned above, nanofibril self-assemblies can facilitate the formation of a continuous and porous network, thereby facilitating their application in gas sensing. Moreover, solution-based self-assembly is available to construct heterojunction nanofibers having the potential to further improve the detection selectivity and sensitivity. Since 2005, our group has performed self-assembly of PTCDIs into 1D nanostructures and explored their wide range of optoelectronic applications due to their unique features.[21,29] On one hand, an n–p dioctyl PTCDI (PTCDI-C8)/copper phthalocyanine (CuPc) heterojunction ultrathin film was used in FET sensors for detection of NO_2.[42] On the other hand, the extraordinary unique features of PTCDI-based heterojunction nanofibers have been emphasized for optoelectronic applications. In contrast to typical electrical current or resistance signals, light is used as the stimulus generating photocurrent to confer conductivity to the highly resistive nanofibril self-assemblies. Even though the photoconductivity of such 1D nanofibers was quite poor (10^{-1}–10^{2} nA measured under a bias voltage of *ca.* 10 V), conductive pathways are realized through the noncovalent columnar π–π stacking between the molecular planes of PTCDIs and continuous covalent π-conjugated pathways in ICPs, MOSs, and SWCNTs. The sensing signals were measured with photocurrent *I*–*t* curves using a probe station in most times. With the help of precise molecular design (*e.g.*, building intramolecular D–A covalent action within PTCDI) of nanofibers and optimal interfacial engineering to tune intermolecular noncovalent heterojunctions between A-type PTCDIs and D-type counterparts, such heterojunctions have exhibited much more promising photoconductive ICT performances. A typical example was alkyl-modified carbazole oligomer (Fig. 19a) or alkoxyl-modified tribenzopentaphene (TBP, Fig. 19b) coated alkyl-modified PTCDI nanofibers.[95,96] The presence and similarity of flexible side-chains attached on both D-type and A-type semiconductor molecules played primary roles in maintaining

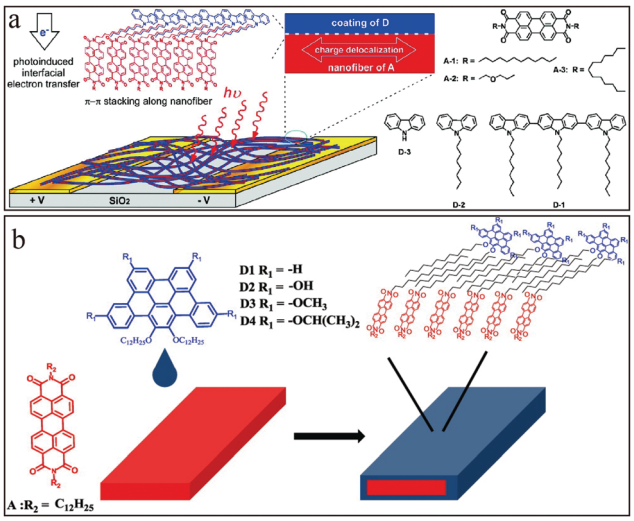

Fig. 19 Schematic illustration of assembled nanofibril heterojunctions for photoconductors employing PTCDI-based configurations in the form of (a) D-type alkyl-modified carbazole oligomer-coated and (b) alkoxyl-TBP-coated PTCDI nanofibers. Reproduced with permission from ref. 95 and 96, copyright 2011 and 2013 American Chemical Society, respectively.

their regular self-assembly after using the simple drop-casting method to construct uniform nanofibril heterojunctions through interfacial hydrophobic interdigitation between alkyl chains (Fig. 19). Solvent vapor annealing can be seen as a good way to achieve homogeneous aggregation and tune the photocurrent transformation.[96] Unlike electrical conductivity, photoconductivity exhibits rapid response times within *ca.* several hundred milliseconds and reversibility with high light-driven on/off ratios up to 10^{4}.[21,96] Under photo-irradiation, charges are generated and they delocalize or migrate along the well-confined nanofibril long axis and separate across the D–A interfaces driven by the disparity of the energy levels between the two materials. In conjunction with spatial phase-separation at the interface and in some cases with side-chain steric-hindrance inhibited intermolecular stacking, such bulk heterojunctions severely inhibit the recombination of photogenerated charges (electrons and holes) in continuous conjugated systems, an inevitable problem for ICPs. Furthermore, the adsorption of oxidative vapor species on the surfaces of n-type PTCDI molecules will withdraw electrons from them and then result in decreased photocurrent. Conversely, p-type semiconductors have depleted hole concentrations upon exposure to reductive vapor. Consequently, their composites can be sensitive to many analytes, with ppt LDLs along with milliseconds response.[21]

Beyond photoexcited ICT, another stimulus that increases the electrical conductivity of PTCDI nanofibers is interfacial interaction similar to the above-mentioned swelling effect that paves its way to CRSs for inactive gases.[21,29] In most cases, such noncovalent interactions at interfaces make these sensors able to detect gases by employing variable lengths of molecular chains to confer sensitivity to low concentrations of an inert gas or VOCs like petro-alkanes at r.t. Because these chemicals cannot participate in interfacial redox actions to give electrical

signals through the normal charge transfer mechanism, such organic/organic nanofibril heterojunctions overcame the challenge of their room-temperature detection. Since our previous two reviews in 2015 provided concise summaries of these topics,[21,29] here we only provide a brief comment about their ICT mechanisms according to controllable molecular structures and interfacial conformations, specially focusing on new progress for developing high-performance alkane sensors that have emerged in the past five years.

In general, depending on the "like dissolves like" interaction between matched side-chains within assemblies and analytes through van der Waals force and the possible solubility of component molecules, the concept was applied to sensing various alkanes from common reagent vapors.[29,97] Moreover, the exciton diffusion lengths (*ca.* 250 nm) confined within the principal axis of the PTCDI nanofiber are dozens of times longer than those in ICPs at r.t. due to the inhibition of back charge recombination. The electrical signals before and after capturing targeted vapor can be tuned through functional chemistry of the D- or A-type conjugated molecules and heterojunction architectures to achieve the most optimal configuration. A fast recovery can be obtained after removing the vapor and is conducive to real-time sensing in mini-devices under room conditions.

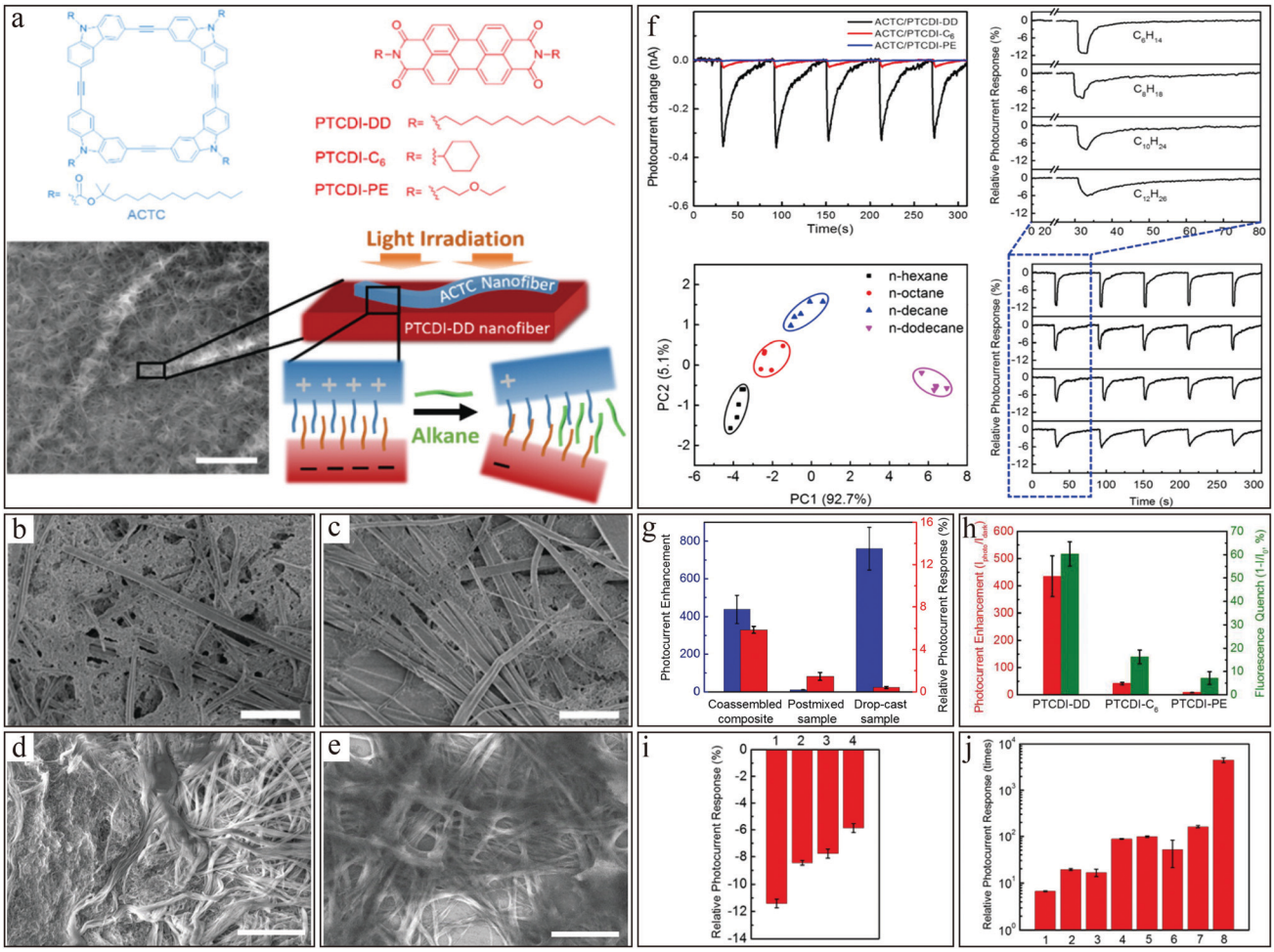

Fig. 20 Schematic illustration of assembled nanofibril heterojunctions for CRSs employing ACTC/PTCDI-DD configurations.[97] (a) Molecular structures of ACTC and alkyl-substituted PTCDIs, a SEM image (scale bar = 3 μm) of ultrathin ACTC fibers attached onto the larger PTCDI fibers and a diagram showing the alkane sensing mechanism based on the tunable ICT process. SEM images (scale bar = 5 μm) of (b) ACTC/PTCDI-C6 and (c) ACTC/PTCDI-PE co-assembly, (d) postmixture of PTCDI-DD nanofibers and ACTC nanofibers, and (e) PTCDI-DD nanofibers covered with subsequently drop-cast ACTC molecules. (f) Photocurrent change comparison of ACTC/PTCDIs upon exposure to saturated *n*-dodecane vapor at r.t., and relative photocurrent response of ACTC/PTCDI-DD (molar ratio 1 : 2) to time curves measured at r.t. for saturated vapors of *n*-hexane (1.6×10^5 ppm), *n*-octane (1.0×10^4 ppm), *n*-decane (2.1×10^3 ppm), and *n*-dodecane (2.2×10^2 ppm). The relative photocurrent response is defined as $(1 - I_t/I_0) \times 100\%$, where I_t is the photocurrent at time *t* and I_0 is the photocurrent at time zero. The principal component scores for the responses of the exposures to the four alkanes (5 trials for each alkane). (g) Comparison of the relative photocurrent responses upon exposure to saturated vapor of dodecane (red) and photocurrent enhancements (blue) among the three morphologies of the ACTC/PTCDI-DD composites. (h) Comparison of fluorescence quenching (green) and photocurrent enhancement (red) for ACTC/PTCDI-DD (1 : 2), ACTC/PTCDI-C6 (1 : 3) and ACTC/PTCDI-PE (1 : 2). General selectivity of the ACTC/PTCDI-DD composite sensor upon exposure to saturated vapors of (i) *n*-hexane (1), *n*-octane (2), *n*-decane (3) and *n*-dodecane (4), and (j) ethanol (1), acetonitrile (2), tetrahydrofuran (3), ethyl acetate (4), dichloromethane (5), water (6), acetone (7) and hexylamine (8), at r.t. Reproduced from ref. 97, copyright 2016 American Chemical Society.

Considering the above aspects, our group provided a comprehensive research study on aryleneethynylene tetracycles (ACTCs)/PTCDIs with special nanofibril conformations as shown in Fig. 20a, where D-type ACTC nanofibers with smaller sizes uniformly covered the surfaces of the PTCDI nanofibers *via* solution-phase co-assembly.[97] Among them, ACTC/PTCDI-DD (the mole ratio was 1 : 2) showed uniform heterojunctions (Fig. 22a) at the D/A interface due to the good dispersion of ACTC nanofibers on PTCDI-DD relying on the compatibility between their similar long alkyl chains in contrast to ACTC/PTCDI-C6 (Fig. 20b) and ACTC/PTCDI-PE (Fig. 20c), and consequently the largest degree of photocurrent enhancement in contrast to PTCDI-DD nanofibers. The same effect occurred for this ordered coassembly method compared to simple post-mixed (Fig. 20d) or drop-casting (Fig. 20e) fabrication, representing a nonporous (deteriorated vapor access) or phase-separated (interrupted D–A interface) conformation, respectively. Also, ACTC/PTCDI-DD exhibited not only favorable adsorption for *n*-dodecane at the alkyl-chain-interdigitated D/A interface and slow diffusion into the porous network, but also difficult dissociation. In contrast, short-chain alkanes like *n*-hexane had higher saturated vapor concentrations, resulting in faster recovery times.

Hence, when used in CRSs, ACTC/PTCDI-DD nanofibers showed unique selectivity and rapid response to *n*-dodecane with a LDL below 1% of its saturated vapor concentration at r.t. (Fig. 20f). The effects of fabrication methods (Fig. 20g) and types of PTCDIs (Fig. 20h) on the initial photocurrents were demonstrated. The outstanding detection signals were from tunable photoinduced ICT from an initial high photocurrent to a sharp decrease. In contrast to the photocurrent of PTCDI-DD nanofibers of *ca.* 35 pA at 15 V, the photocurrent of ACTC/PTCDI-DD nanofibers was *ca.* 950 pA (about 430 times higher than their dark current) which decreased by about 6 or 12 times upon exposure to saturated vapor of *n*-dodecane (2.2×10^2 ppm) or *n*-hexane (1.6×10^5 ppm), respectively. Also, this sensor yielded a similar response but faster recovery for *n*-hexane (1.7 s) than *n*-dodecane (11 s) and other long alkanes (Fig. 20i). In contrast, an opposite phenomenon (Fig. 20j), *i.e.*, photocurrent enhancement, was observed for this sensor upon its exposure to common reagent vapors based on the typical ICT mechanism. For example, for an analyte like hexylamine that possesses both alkyl chain and a redox active group, significant enhancement of photocurrent was observed due to the dominant role played by the ICT mechanism.

Nevertheless, such nanofibril bulk-heterojunction sensors are very appropriate to selectively detect alkanes while responding with the opposite polarity to common polar gases; however, molecular self-assembly usually generated much smaller nanofibers (several to hundreds of micrometers long and tens of nanometers wide) than other techniques and such nanofibers could exhibit relatively poor mechanical properties. To realize their further development, it is necessary to explore the underlying mechanisms, and the molecular versatility of PTCDIs together with elaborate heterojunction control. For instance, through design of covalent D–A oligomers from oligothiophenes and PTCDIs with tailored interfacial p/n heterojunctions, self-assembled nanofibers

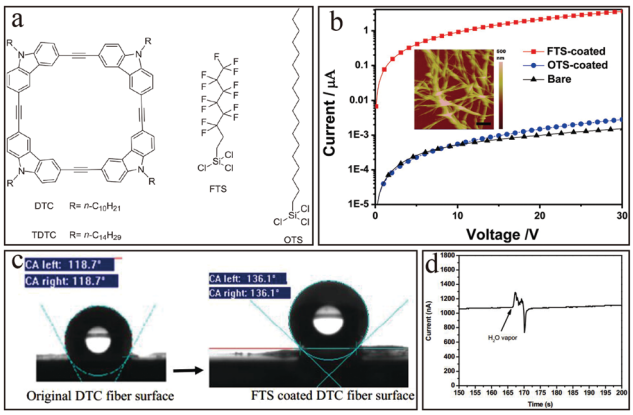

Fig. 21 (a) Molecular structures of DTC, TDTC, FTS, and OTS. (b) Current–voltage (*I*–*V*) curves for bare, OTS-, and FTS-coated DTC nanofibers, and atomic force microscopy (AFM) images of DTC fibers after FTS coating. (c) Contact angle measurements of pristine and FTS modified DTC nanofibers. FTS treatment increased the contact angle from 118° to 136°.[92] (d) Electrical current measured over the FTS modified DTC nanofibers upon exposure to saturated H_2O vapor (23 000 ppm). Adapted and reproduced from ref. 92, copyright 2013 American Chemical Society.

of oligothiophene–PTCDI dyads *via* amphiphilic side-chain incompatibility exhibited good photoconductive properties.[98] This research draws our attention because of its capability to extend the types of analytes that can be detected. Indeed, for the optimal intrinsic current of D/A interfacial heterojunction nanofibers without photo-irradiation, namely dark electrical conductivity, a conventional CRS with a reliable signal-to-noise ratio can also be realized.[92] By surface coating A-type (tridecafluoro-1,1,2,2-tetrahydrooctyl)trichlorosilane (FTS) molecules onto the networks of assembled D-type carbazole-cornered aryleneethynylene tetracyclic molecule (DTC) nanofibers (Fig. 21a), the heterojunction nanofibers can achieve electrical current values around 1 μA measured under bias voltages of 10–30 V (Fig. 21b).[92] The high current was due to the high electron affinity of FTS and strong ICT between A and D, in addition to the subsequent charge delocalization along the 1D long axis of the DTC nanoassemblies. Upon exposure to NH_3 vapor, the sensor showed a chemiresistive sensing behavior, with the decreased current signal arising from the electron transfer from the NH_3 to FTS and reduction in the density of holes in the DTC nanofibers. The high selectivity with a quite low LDL of 0.38 ppb together with a short response time of 2.8 s made the sensor more efficient than others. Promisingly, the hydrophobic FTS surface may provide resistance to humidity (Fig. 21c and d).

4. Conclusions

In summary, efficient ICT was presented as the vital prerequisite for high-performance chemiresistive gas sensors. The mechanisms through which nanofibril heterojunctions participate in sensing behaviors have been discussed in relation to variations of tunable compositions, architectures, interfacial activity, *etc.* Briefly, a summary about the recent developments of various nanofibril heterojunctions constructed from MOSs, ICPs, molecular assemblies and carbon materials was provided.

Although inorganic/inorganic nanofibril heterojunctions have issues like high-temperature of fabrication and operation, those materials are viable for surface modification with catalytic functionalization (in order to improve the sensor response and selectivity), and thus still remain as great choice for detecting H_2, NH_3, solvent vapors or other normal gaseous analytes. In contrast, for inorganic/organic types, the operation at r.t. and specific responses to NH_3, nitro compounds and inert alkanes were addressed. However, their relatively lower responses, longer response times and interface incompatibility will prohibit their real applications. Only polymers/SWCNTs seem quite promising for r.t. detection with low LDLs in security fields, benefiting from intrinsic superiority of SWCNTs and devisable polymer structures. Moreover, easily tunable architectures *via* facile fabrication with unique interfacial interaction and rapid response at r.t. make organic/organic type sensors attractive for future applications, especially D/A semiconductor composites, and for flexible and portable CRSs. But their selectivity and comprehensive stability are still far from realizing a broad range of applications. Nevertheless, when employed in real environment, all the sensors mentioned above should still address the common interference from humidity and oxygen, which often cause significant effect (*e.g.*, signal fluctuation, baseline drift) to the sensor performance.

Apart from the particular emphasis on building efficient nanofibril heterojunction interfaces, recent advances in improving material morphologies for controlled adsorption and desorption of a specific gas molecule to identify it in a complex environment were also mentioned. The sensing performances usually originate from a synergistic mechanism; enhancing one parameter while increasing or maintaining another is still a challenge. Consequently, the exciting features and tunable structures of nanofibril heterojunctions will continually promote their wide use in sensors and a great deal of effort is still required to understand the mechanisms governing their behavior.

5. Outlook

As described above, extensive theoretical and experimental studies to develop nanofibril heterojunctions for CRSs have been performed on MOS nanofibers and their composites with another MOS or ICP, as well as pure organic bulk heterojunctions, which can work at r.t. in portable instruments. Many challenges remain to construct nanofibril heterojunctions that can exhibit excellent ICT behaviors and relatively better selectivity, long-term stability, and durability. Thus, it is necessary to expand our understanding of such sensors, especially considering the rapid development of flexible and stretchable sensors for wearable electronics,[99,100] e-skins,[101,102] soft robotics,[100,103] implantable chips,[104] or other human–machine interface devices.[105] Herein, we intend to give future perspectives and some insights to address the above-mentioned issues and challenges.

5.1 Flexible, portable CRSs

The foremost challenge to realizing a flexible sensor is attaching an active material to a flexible electrode substrate. Recently, remarkable advances were achieved through directly grown (*e.g.*, electrodeposition, *in situ* synthesis) or post-transferred (*e.g.*, drop-casting, polydimethylsiloxane (PDMS) stamping) sensor materials on various plastic substrates with thermal and chemical resistance and mechanical robustness such as polyimide (PI), polyethylene terephthalate (PET), and PDMS, and cost-effective fabric textiles or paper.[19,99,104,106–109] In contrast to the low activity of carbon materials and MOS nanoparticles at r.t.,[105] use of heterojunction nanofibers has the potential to address these limitations. A flexible CRS was fabricated by coating 2D/1D Bi_2WO_6/TiO_2 heterostructure nanofibers

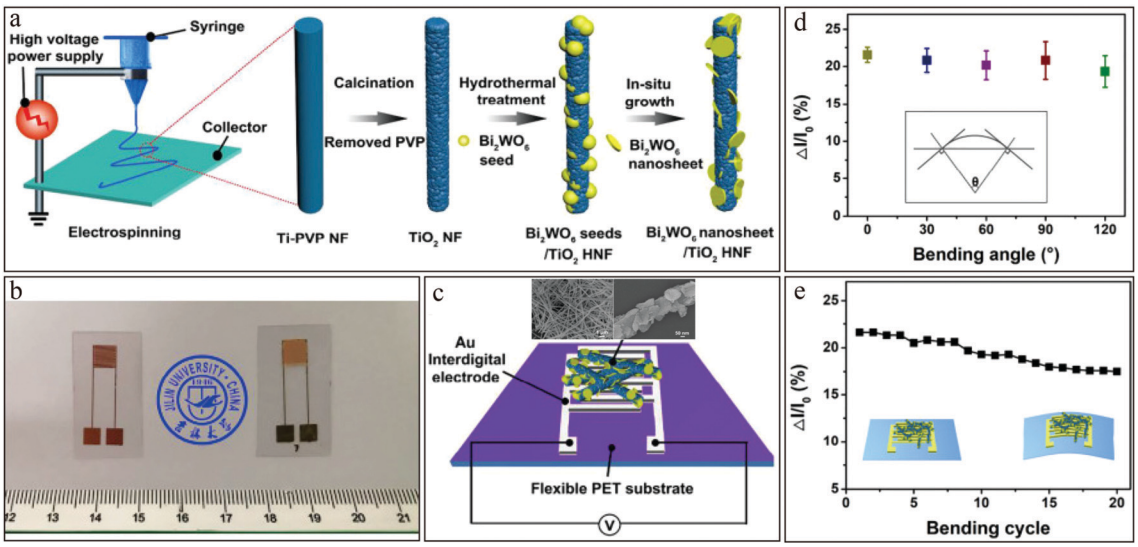

Fig. 22 Flexible CRSs based on 2D/1D Bi_2WO_6/TiO_2 heterojunction nanofibers. (a) Proposed scheme for the fabrication. (b) Optical images of blank and Bi_2WO_6/TiO_2-based flexible sensing devices. (c) Schematic sensor and measurement configurations, and FESEM images of Bi_2WO_6/TiO_2. (d) Sensitivity and (e) long-term stability as functions of the bending angle. Adapted and reproduced with permission from ref. 68, copyright 2019 Elsevier B.V.

onto a 60 μm-thick PET substrate with a Au interdigitated electrode (Fig. 22a–c).[68] This sensor was highly sensitive to ethanol gas to realize real-time detection at r.t., and exhibited mechanical stability during repeated bending (Fig. 22d and e).

Beyond interior ICT, much improved interfacial contact between the sensing materials and electrodes is critically important in determining the overall sensor behavior.[4] A well-known ICP, PEDOT:poly(styrenesulfonate) (PEDOT:PSS), holds great potential as an active electrode material (as a rival to brittle and expensive ITO), due to its solution-processability, flexible properties, and high electrical conductivity. Such conductive films of polymer chain networks could provide favorable surfaces to make contact with nanofibril heterojunction sensing materials and gas analytes. This provides the potential to construct all-organic flexible gas sensors.

As before, PEDOT:PSS membrane composites with Ag, Cu, Fe, or graphene have been used for detecting 100 ppm NH_3, CO, or H_2, with the response/recovery times ranging from several to tens of seconds.[36] For example, a flexible NH_3 sensor for monitoring the freshness of pork under concentrations below 0.5 ppm was fabricated on a PET substrate using a PEDOT:PSS/silver nanowire composite film as the active layer.[110] Recently in 2018, high-performance electronic noses (e-noses) were constructed in the form of arrays of sensors based on PEDOT:PSS nanowires with sub-100 nm diameters fabricated using low-cost nanoscale soft lithography (Fig. 23a and b).[111] Their excellent sensitivity and selectivity to ten VOCs including ketones, alcohols, alkanes, aromatics, and amines (Fig. 23c) arose from the addition of four self-assembled monolayers (SAMs) of perfluorooctyl, octadecyl, 3-aminopropyl, and 3-bromopropyl functional groups (Fig. 23a). Selective sensor responses were achieved by tuning the swelling effect of the PEDOT:PSS nanofibers because of the different levels of polarity of side-chains. For example, long-chain alkylated OTES favored hydrocarbon dispersion interactions with alkane analytes, quite similar to the PTCDI-based nanofibril CRSs presented earlier.

In this regard, we propose that combining n-type PTCDI nanofibers or heterojunctioned nanofibers in the gaps or on the surfaces of p-type PEDOT:PSS nanowires on flexible films, with the help of air plasma treatment as shown in Fig. 23, could enable a new process for mass producing next-generation all-organic flexible sensors. Furthermore, just like a pH test strip where cheap paper is used as a disposable substrate, by coating organic heterojunction nanofibers onto a paper substrate, a disposable chemical sensor can be achieved.

In spite of the advantages, the construction of stable device interfaces on flexible substrates is still a challenge. The attachment of heterojunction nanofibers obtained from ICPs or PTCDIs with graphene or SWCNT films may be another attractive choice. They can form stable interfacial binding *via* covalent or non-covalent interactions. Also, one or more additional heterojunctions within a sensing layer can be formed, resulting in high performances.

5.2 Humidity resistance

Portable breath analysis based on simple and low-cost CRSs is attractive for point-of-care testing, as it provides quick, non-invasive disease diagnosis. However, for breath analysis or chemical detection in a real environment, minimizing the effect of humidity on interfacial adsorption and ICP processes

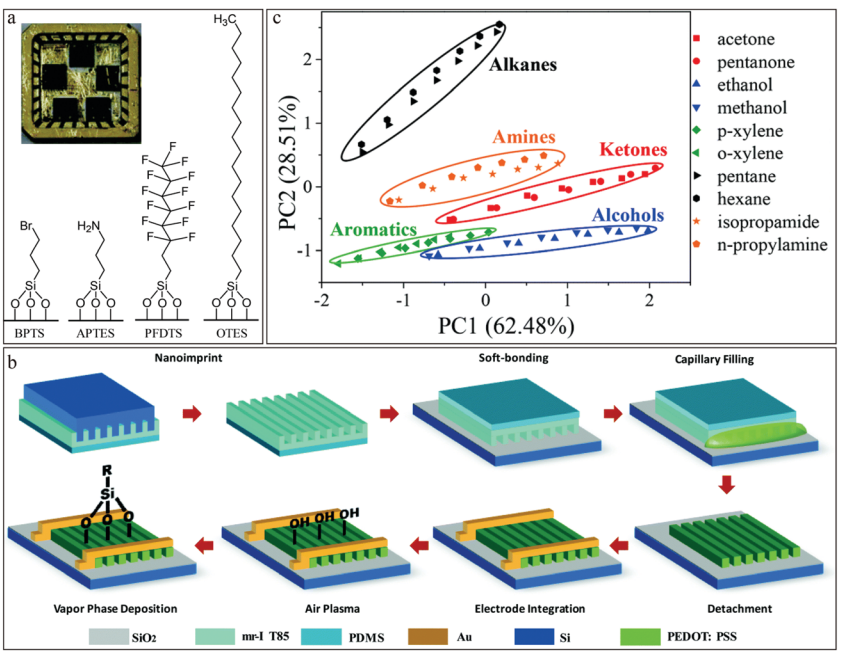

Fig. 23 E-nose based on a pattern recognition algorithm and SAM-modified PEDOT:PSS nanowire CRS arrays. (a) Photo of senor arrays and structures of SAM layers attached to the PEDOT:PSS nanowire surfaces. (b) Schematic of the fabrication process through low-cost nanoscale soft lithography. (c) Statistical analysis of the sensor array's responses. PC2 plotted against PC1 for the sensor array to 5 types of VOCs with seven different concentrations ranging from 800 ppm to 2000 ppm.[111] Reproduced with permission from ref. 111, copyright 2018 Royal Society of Chemistry.

significantly hinders CRSs' applications. Recent studies of PEDOT:PSS in electronic devices show that the material should be sealed from the contact with atmosphere because of the strong hydrophilicity of PSS. In studying the humidity effect on NH_3 detection, thin films of a histidine substituted PTCDI were fabricated as effective CRSs working in a wide range of humidity, with a LDL of 0.56 ppm.[112] Beyond the material choice and structural design of nanofibril heterojunctions, exterior humidity control integrated into a sensor instrument is another approach.

5.3 Cross-sensitivity

The cross-sensitivity towards different gaseous molecules in complex external environments is another critical problem for CRSs, although MOSs offer a little improvement at optimal high temperatures.[6] A great deal of effort has been devoted to developing heterojunction nanofibers with tunable ICT, resulting in much higher or lower initial resistance, which represents an elevated signal-to-noise ratio (*i.e.*, better selectivity and sensitivity). However, recent devices were still short of the goal of detecting multiple analytes and distinguishing an individual from the others. Thus, rather than extensive research on single sensor devices, more vigorous investigations of the integration of homologous or heterogeneous nanofibril heterojunction CRSs into arrays in microelectronic devices in combination with the corresponding pattern recognition systems are required. Inspired by the development of e-noses providing fingerprints for odor discrimination,[12,113] as the example shown in Fig. 23, improvements in this area can be expected. Indeed, an instrument named PILOT™ that employs PTCDI nanofiber-based sensor arrays for enhanced identification of gaseous-phase chemicals has been developed by Vaporsens, Inc., a company focusing on the development of ultrasensitive nanofiber chemical sensors spun off from our lab. It is believed that this instrument with further optimization may pave the way for developing portable sensors for real-time breath analysis of tremendous amounts of gaseous species under levels ranging from several ppt to several ppm.[13]

Nevertheless, there are still severe issues like limited mass production and reliability for array-based devices. It is necessary to recalibrate the pattern recognition system for every sensor array. This is also the reason why research on sensor arrays with different individual sensors based on diverse heterojunction materials is scarce. Furthermore, the issue and challenge of drift must be addressed to eliminate the requirement of frequent recalibration or replacement of sensors.

5.4 Multimodal sensing

Despite the significant progress in sensors with multifunctionalization like catalysis, there is still much to be explored for multimodal sensing *via* integration of conductometric, colorimetric, or other responses, to enhance the broad adaptability of one sensor for diverse stimulating environments.[8,114] In this aspect, ICPs have unique advantages due to their variety of abundant optoelectronic capabilities. Their electrochromism is of special interest because it is a zero or low power consuming phenomenon analogous to electric current change, which is also caused by tunable chemical doping. Among the different types, PThs not only show good sensor performance but also show better stability against oxidation and humidity than PANI and PPy. The above-mentioned PEDOT:PSS thin-films with good optical modulation from almost transparent (doped) to blue (neutral) offer great potential as a platform for supporting nanofibril heterojunction materials to obtain bimodal flexible chemosensors operating at r.t.

5.5 Printing, micro-patterning, and chemitransistor CRSs

Apart from materials and structures, modern electronic technologies will open a new era to explore high-performance nanofibril heterojunction CRSs. Printing sensing platforms onto plastic substrates is suitable to fabricate flexible or stretchable sensors.[106] Printable organic nanofibril heterojunctions have not yet been realized on a large scale because recent materials nearly all utilize delicate structures that may be destroyed by the traditional printing process. At present, inkjet-printing technology is most applicable to carbon materials or ICP-based composites which are solution-processable at low temperatures.[115] Alternatively, micro-patterning of electrospun MOS nanofibers or heterogeneous arrays on microelectrodes with microheaters has been demonstrated as a useful technology for multiplexed parallel detection of multiple target toxic gases such as NO_2, CO, and H_2S.[116] Furthermore, as another class of promising gas sensors relying on electrical transduction signals, chemical field effect transistors (chemFETs) show a great signal amplification effect *via* gate voltage tuning closely tied to high sensitivity and a low LDL.[4,13,16,117] For further widening the application range of nanofibril heterojunctions, their combination with FETs or organic thin film transistors (OTFTs) will be of increased interest.[10,16,118]

Notably, in addition to the above-mentioned choice of film electrode material, suitable fabrication technologies not only can control material morphologies and architectures, but can also optimize the ohmic contact between sensing nanofibers and supporting electrodes.[119]

In conclusion, heterojunction nanofibers in sensor arrays are a promising class of materials to achieve high-performance sensors that are suitable for applications in ambient environments. Undoubtedly, a deep understanding of the ICT mechanisms along with precisely tunable nanoscale heterojunctions in every individual sensor is a basic requirement that deserves more attention. Beyond general interface characterization techniques such as scanning probe imaging, UV-vis, photoluminescence, X-ray, AFM and Raman spectroscopies, unusual or new strategies (*e.g.*, lateral force, electrostatic force, scanning ultrasound and Kelvin probe force microscopies) are constantly emerging and may provide great help to analyze the nanostructure and morphology of interface,[120–123] and should be taken more attentions.

Conflicts of interest

There are no conflicts to declare.

Acknowledgements

All individual contributions in the cited references are gratefully acknowledged, and any omission is deeply apologized. We

gratefully acknowledge financial support from the National Natural Science Foundation of China (No. 51603095), the China Scholarship Council (No. 201808360327), the Natural Science Foundation of Jiangxi Province (No. 20192BAB216012), and the Scientific Fund of Jiangxi Science & Technology Normal University (No. 2016QNBJRC003).

Notes and references

1 S. Kumar, V. Pavelyev, P. Mishra and N. Tripathi, *Sens. Actuators, A*, 2018, **283**, 174.
2 A. Chidambaram and K. C. Stylianou, *Inorg. Chem. Front.*, 2018, **5**, 979.
3 I. Fratoddi, I. Venditti, C. Cametti and M. V. Russo, *Sens. Actuators, B*, 2015, **220**, 534.
4 C. M. Hangarter, N. Chartuprayoon, S. C. Hernández, Y. Choa and N. V. Myung, *Nano Today*, 2013, **8**, 39.
5 E. Song and J.-W. Choi, *Nanomaterials*, 2013, **3**, 498.
6 S. Pandey, *J. Sci.: Adv. Mater. Devices*, 2016, **1**, 431.
7 F. Meng, Z. Guo and X. J. Huang, *Trends Anal. Chem.*, 2015, **68**, 37.
8 S. J. Choi, L. Persano, A. Camposeo, J. S. Jang, W. T. Koo, S. J. Kim, H. J. Cho, I.-D. Kim and D. Pisignano, *Macromol. Mater. Eng.*, 2017, **302**, 1600569.
9 N. Ramgir, N. Datta, M. Kaur, S. Kailasaganapathi, A. K. Debnath, D. K. Aswal and S. K. Gupta, *Colloids Surf., A*, 2013, **439**, 101.
10 G. T. Chandran, X. W. Li, A. Ogata and R. M. Penner, *Anal. Chem.*, 2017, **89**, 249.
11 S. J. Kim, S. J. Choi, J. S. Jang, H. J. Cho and I.-D. Kim, *Acc. Chem. Res.*, 2017, **50**, 1587.
12 A. H. Jalal, F. Alam, S. Roychoudhury, Y. Umasankar, N. Pala and S. Bhansali, *ACS Sens.*, 2018, **3**, 1246.
13 N. Nasiri and C. Clarke, *Sensors*, 2019, **19**, 462.
14 R. X. Tang, Y. J. Shi, Z. Y. Hou and L. M. Wei, *Sensors*, 2017, **17**, 882.
15 V. Schroeder, S. Savagatrup, M. He, S. Lin and T. M. Swager, *Chem. Rev.*, 2019, **119**, 599.
16 A. Mohtasebi and P. Kruse, *Phys. Sci. Rev.*, 2018, 20170133.
17 S. Y. Chen, Y. L. Tang, K. Zhan, D. H. Sun and X. Hou, *Nano Today*, 2018, **20**, 84.
18 J. F. Fennell Jr., S. F. Liu, J. M. Azzarelli, J. G. Weis, S. Rochat, K. A. Mirica, J. B. Ravnsbæk and T. M. Swager, *Angew. Chem., Int. Ed.*, 2016, **55**, 1266.
19 A. Chinnappan, C. Baskar, S. Baskar, G. Ratheeshd and S. Ramakrishna, *J. Mater. Chem. C*, 2017, **5**, 12657.
20 Y. Z. Long, M. M. Li, C. Z. Gu, M. X. Wan, J. L. Duvail, Z. W. Liu and Z. Y. Fan, *Prog. Polym. Sci.*, 2011, **36**, 1415.
21 S. Chen, P. Slattum, C. Y. Wang and L. Zang, *Chem. Rev.*, 2015, **115**, 11967.
22 R. S. Andre, R. C. Sanfelice, A. Pavinatto, L. H. C. Mattoso and D. S. Correa, *Mater. Des.*, 2018, **156**, 154.
23 M. Mittal and A. Kumar, *Sens. Actuators, B*, 2014, **203**, 349.
24 D. R. Miller, S. A. Akbar and P. A. Morris, *Sens. Actuators, B*, 2014, **204**, 250.
25 T. M. Li, W. Zeng and Z. C. Wang, *Sens. Actuators, B*, 2015, **221**, 1570.
26 Q. Y. Li, S. Ding, W. G. Zhu, L. L. Feng, H. L. Dong and W. P. Hu, *J. Mater. Chem. C*, 2016, **4**, 9388.
27 X. M. Feng, G. Q. Hu and J. Q. Hu, *Nanoscale*, 2011, **3**, 2099.
28 F. S. Kim, G. Q. Ren and S. A. Jenekhe, *Chem. Mater.*, 2011, **23**, 682.
29 L. Zang, *Acc. Chem. Res.*, 2015, **48**, 2705.
30 B. Rezek, J. Čermák, A. Kromka, M. Ledinský, P. Hubík, J. J. Mareš, A. Purkrt, V. Cimrová, A. Fejfar and J. Kočka, *Nanoscale Res. Lett.*, 2011, **6**, 238.
31 O. Ostroverkhova, *Chem. Rev.*, 2016, **116**, 13279.
32 A. D. Bartolomeo, *Phys. Rep.*, 2016, **606**, 1.
33 W. S. Xia, L. P. Dai, P. Yu, X. Tong, W. P. Song, G. J. Zhang and Z. M. Wang, *Nanoscale*, 2017, **9**, 4324.
34 Z. M. Zhang, Y. Ning and X. S. Fang, *J. Mater. Chem. C*, 2019, **7**, 223.
35 S. Xu, D. F. Fu, K. Song, L. Wang, Z. B. Yang, W. Y. Yang and H. L. Hou, *Chem. Eng. J.*, 2018, **349**, 368.
36 L. Zhang, W. Y. Du, A. Nautiyal, Z. Liu and X. Y. Zhang, *Sci. China Mater.*, 2018, **61**, 303.
37 S. Chen, D. L. Jacobs, J. K. Xu, Y. X. Li, C. Y. Wang and L. Zang, *RSC Adv.*, 2014, **4**, 48486.
38 S. Chen, C. Wang, B. R. Bunes, Y. X. Li, C. Y. Wang and L. Zang, *Appl. Catal., A*, 2015, **498**, 63.
39 L. G. Li, D. L. Jacobs, B. R. Bunes, H. L. Huang, X. M. Yang and L. Zang, *Polym. Chem.*, 2013, **5**, 309.
40 Z. Y. Wang, J. Hai, T. R. Li, E. Ding, J. X. He and B. D. Wang, *ACS Sustainable Chem. Eng.*, 2018, **6**, 9921.
41 K. B. Paul, S. Kumar, S. Tripathy, S. R. K. Vanjari, V. Singh and S. G. Singh, *Biosens. Bioelectron*, 2016, **80**, 39.
42 H. D. Fan, W. Shi, X. G. Yu and J. S. Yu, *Synth. Met.*, 2016, **211**, 161.
43 J. H. Kim, J. H. Lee, A. Mirzaei, H. W. Kim and S. S. Kim, *Sens. Actuators, B*, 2017, **248**, 500.
44 Y. Wang, A. Maity, X. Y. Sui, H. H. Pu, S. Mao, N. K. Singh and J. H. Chen, *ACS Omega*, 2018, **3**, 18685.
45 J. H. Lee, J. Y. Kim, A. Mirzaei, H. W. Kim and S. S. Kim, *Nanomaterials*, 2018, **8**, 902.
46 Y. Q. Liang, Z. D. Cui, S. L. Zhu, Z. Y. Li, X. J. Yang, Y. J. Chen and J. M. Ma, *Nanoscale*, 2013, **5**, 10916.
47 N. Kaur, D. Zappa, M. Ferroni, N. Poli, M. Campanini, R. Negrea and E. Comini, *Sens. Actuators, B*, 2018, **262**, 477.
48 B. Y. Huang, Z. X. Zhang, C. H. Zhao, L. Cairang, J. L. Bai, Y. X. Zhang, X. M. Mu, J. W. Du, H. Wang, X. J. Pan, J. Y. Zhou and E. Q. Xie, *Sens. Actuators, B*, 2018, **255**, 2248.
49 P. X. Zhao, Y. Tang, J. Mao, Y. X. Chen, H. Song, J. W. Wang, Y. Song, Y. Q. Liang and X. M. Zhang, *J. Alloys Compd.*, 2016, **674**, 252.
50 Y. X. Qin, X. J. Zhang, Y. Liu and W. W. Xie, *J. Alloys Compd.*, 2016, **673**, 364.
51 Z. Q. Li, P. Song, Z. X. Yang and Q. Wang, *Ceram. Int.*, 2018, **44**, 3364.
52 X. Q. Qiao, Z. W. Zhang, D. F. Hou, D. S. Li, Y. L. Liu, Y. Q. Lan, J. Zhang, P. Y. Feng and X. H. Bu, *ACS Sustainable Chem. Eng.*, 2018, **6**, 12375.

53 S. Yana, J. Z. Xue and Q. S. Wu, *Sens. Actuators, B*, 2018, **275**, 322.
54 L. W. Wang, J. T. Li, Y. H. Wang, K. F. Yu, X. Y. Tang, Y. Y. Zhang, S. P. Wang and C. S. Wei, *Sci. Rep.*, 2016, **6**, 35079.
55 J. H. Kim, A. Mirzaei, Y. F. Zheng, J. H. Lee, J. Y. Kim, H. W. Kim and S. S. Kim, *Sens. Actuators, B*, 2019, **281**, 453.
56 J.-M. Choi, J. H. Byun and S. S. Kim, *Sens. Actuators, B*, 2016, **227**, 149.
57 A. Katoch, Z. U. Abideen, H. W. Kim and S. S. Kim, *ACS Appl. Mater. Interfaces*, 2016, **8**, 2486.
58 Y. J. Sun, Z. P. Wang, W. D. Wang, G. Li, P. W. Li, K. Lian, W. D. Zhang, S. Zhuiykov, J. Hu and L. Chen, *Mater. Res. Bull.*, 2019, **109**, 255.
59 K. C. Hsu, T. H. Fang, S. H. Chen and E. Y. Kuo, *Ceram. Int.*, 2019, **45**, 8744.
60 C. S. Lee, H. Y. Li, B. Y. Kim, Y. M. Jo, H. G. Byun, I. S. Hwang, F. Abdel-Hady, A. A. Wazzan and J. H. Lee, *Sens. Actuators, B*, 2019, **285**, 193.
61 J. Cao, Z. Y. Wang, R. Wang, S. Liu, T. Fei, L. J. Wang and T. Zhang, *RSC Adv.*, 2015, **5**, 36340.
62 J. H. Lee, J. Y. Kim, J. H. Kim and S. S. Kim, *Sensors*, 2019, **19**, 726.
63 A. Queraltó, D. Graf, R. Frohnhoven, T. Fischer, H. Vanrompay, S. Bals, A. Bartasyte and S. Mathur, *ACS Sustainable Chem. Eng.*, 2019, **7**, 6023.
64 L. T. Hoa and S. H. Hur, *Phys. Status Solidi A*, 2013, **210**, 1213.
65 D. D. Chen and J. X. Yi, *J. Nanopart. Res.*, 2018, **20**, 65.
66 Y. J. Chen, G. Xiao, T. S. Wang, F. Zhang, Y. Ma, P. Gao, C. L. Zhu, E. D. Zhang, Z. Xu and Q. H. Li, *Sens. Actuators, B*, 2011, **155**, 270.
67 J. Cao, Z. Y. Wang, R. Wang, S. Liu, T. Fei, L. J. Wang and T. Zhang, *J. Mater. Chem. A*, 2015, **3**, 5635.
68 K. Wang, W. Wei, Z. Lou, H. Zhang and L. Wang, *Appl. Surf. Sci.*, 2019, **479**, 209.
69 Q. Wang, J. L. Bai, B. Y. Huang, Q. Hu, X. Cheng, J. P. Li, E. Q. Xie, Y. R. Wang and X. J. Pan, *J. Alloys Compd.*, 2019, **791**, 1025.
70 J. S. Jang, H. Yu, S. J. Choi, W. T. Koo, J. Lee, D. H. Kim, J. Y. Kang, Y. J. Jeong, H. Jeong and I.-D. Kim, *ACS Appl. Mater. Interfaces*, 2019, **11**, 10208.
71 D. Wang, K. C. Wan, M. L. Zhang, H. J. Li, P. Wang, X. Y. Wang and J. H. Yang, *Sens. Actuators, B*, 2019, **283**, 714.
72 Q. Qi, J. Zhao, R. F. Xuan, P. P. Wang, L. L. Feng, L. J. Zhou, D. J. Wang and G. D. Li, *Sens. Actuators, B*, 2014, **191**, 659.
73 M. Joulazadeh and A. H. Navarchian, *Synth. Met.*, 2015, **210**, 404.
74 R. K. Jha, M. Wan, C. Jacob and P. K. Guha, *New J. Chem.*, 2018, **42**, 735.
75 Z. Y. Pang, Q. X. Nie, P. F. Lv, J. Yu, F. L. Huang and Q. F. Wei, *Nanotechnology*, 2017, **28**, 225501.
76 J. Jun, J. S. Lee, D. H. Shin, J. Oh, W. Kim, W. Na and J. Jang, *J. Mater. Chem. A*, 2017, **5**, 17335.
77 C. J. Liu, K. Hayashi and K. Toko, *Sens. Actuators, B*, 2012, **161**, 504.
78 Y. Q. Zhang, M. Xu, B. R. Bunes, N. Wu, D. E. Gross, J. S. Moore and L. Zang, *ACS Appl. Mater. Interfaces*, 2015, **7**, 7471.
79 Y. Q. Zhang, B. R. Bunes, C. Wang, N. Wu and L. Zang, *Sens. Actuators, B*, 2017, **247**, 713.
80 Y. Q. Zhang, B. R. Bunes, N. Wu, A. Ansari, S. Rajabali and L. Zang, *Sens. Actuators, B*, 2018, **255**, 1814.
81 B. R. Bunes, M. Xu, Y. Q. Zhang, D. E. Gross, A. Saha, D. L. Jacobs, X. M. Yang, J. S. Moore and L. Zang, *Adv. Mater.*, 2014, **27**, 162.
82 J. F. Fennell Jr., H. Hamaguchi, B. Yoon and T. M. Swager, *Sensors*, 2017, **17**, 982.
83 F. Wang, H. W. Gu and T. M. Swager, *J. Am. Chem. Soc.*, 2008, **130**, 5392.
84 O. S. Kwon, S. J. Park, H. Yoon and J. Jang, *Chem. Commun.*, 2012, **48**, 10526.
85 L. P. C. Júnior, D. B. R. S. S. Silva, M. F. de Aguiar, C. P. de Melo and K. G. B. Alves, *J. Mol. Liq.*, 2019, **275**, 452.
86 V. P. Anju, P. R. Jithesh and S. K. Narayanankutty, *Sens. Actuators, A*, 2019, **285**, 35.
87 Y. Hu, H. Yu, Z. Y. Yan and Q. F. Ke, *RSC Adv.*, 2018, **8**, 8747.
88 J. Zhu, C. L. Shao, X. H. Li, C. H. Han, S. Yang, J. G. Ma, X. W. Li and Y. C. Liu, *Mater. Chem. Phys.*, 2018, **214**, 507.
89 Z. G. Yin and Q. D. Zheng, *Adv. Energy Mater.*, 2012, **2**, 179.
90 P. Dallas and V. Georgakilas, *Adv. Colloid Interface Sci.*, 2015, **224**, 46.
91 M. J. T. Raaijmakers and N. E. Benes, *Prog. Polym. Sci.*, 2016, **63**, 86.
92 H. L. Huang, D. E. Gross, X. M. Yang, J. S. Moore and L. Zang, *ACS Appl. Mater. Interfaces*, 2013, **5**, 7704.
93 Z. X. Zhang, H. L. Huang, X. M. Yang and L. Zang, *J. Phys. Chem. Lett.*, 2011, **2**, 2897.
94 N. Wu, C. Wang, B. R. Bunes, Y. Q. Zhang, P. M. Slattum, X. M. Yang and L. Zang, *ACS Appl. Mater. Interfaces*, 2016, **8**, 12360.
95 Y. K. Che, H. L. Huang, M. Xu, C. Y. Zhang, B. R. Bunes, X. M. Yang and L. Zang, *J. Am. Chem. Soc.*, 2011, **133**, 1087.
96 H. L. Huang, C.-E. Chou, Y. K. Che, L. G. Li, C. Wang, X. M. Yang, Z. H. Peng and L. Zang, *J. Am. Chem. Soc.*, 2013, **135**, 16490.
97 C. Wang, B. R. Bunes, M. Xu, N. Wu, X. M. Yang, D. E. Gross and L. Zang, *ACS Sens.*, 2016, **1**, 552.
98 W. S. Li, A. Saeki, Y. Yamamoto, T. Fukushima, S. Seki, N. Ishii, K. Kato, M. Takata and T. Aida, *Chem. – Asian J.*, 2010, **5**, 1566.
99 E. Singh, M. Meyyappan and H. S. Nalwa, *ACS Appl. Mater. Interfaces*, 2017, **9**, 34544.
100 M. Y. Xie, K. Hisano, M. Z. Zhu, T. Toyoshi, M. Pan, S. Okada, O. Tsutsumi, S. Kawamura and C. Bowen, *Adv. Mater. Technol.*, 2019, **4**, 1800626.
101 J. B.-H. Tok and Z. N. Bao, *Sci. Chin. Chem.*, 2012, **55**, 718.
102 K. C. Xu, Y. Y. Lu and K. Takei, *Adv. Mater. Technol.*, 2019, **4**, 1800628.
103 S. Li, H. C. Zhao and F. Robert, *MRS Bull.*, 2017, **42**, 138.
104 C. Pang, C. Lee and K. Y. Suh, *J. Appl. Polym. Sci.*, 2013, **130**, 1429.

105 B. Hu, W. Chen and J. Zhou, *Sens. Actuators, B*, 2013, **176**, 522.
106 Y. S. Rim, S. H. Bae, H. J. Chen, N. D. Marco and Y. Yang, *Adv. Mater.*, 2016, **28**, 4415.
107 X. Q. Zheng and H. Y. Cheng, *Sci. China: Technol. Sci.*, 2019, **62**, 209.
108 L. N. Xue, W. Wang, Y. L. Guo, G. Q. Liu and P. B. Wan, *Sens. Actuators, B*, 2017, **244**, 47.
109 S. Kanaparthi and S. G. Singh, *Org. Electron.*, 2019, **68**, 108.
110 S. Y. Li, S. J. Chen, B. G. Zhuo, Q. F. Li, W. J. Liu and X. J. Guo, *IEEE Electron. Device Lett.*, 2017, **38**, 975.
111 Y. Jiang, N. Tang, C. Zhou, Z. Y. Han, H. M. Qu and X. X. Duan, *Nanoscale*, 2018, **10**, 20578.
112 A. Kalita, S. Hussain, A. H. Malik, N. V. V. Subbarao and P. K. Iyer, *J. Mater. Chem. C*, 2015, **3**, 10767.
113 S.-W. Chiu and K.-T. Tang, *Sensors*, 2013, **13**, 14214.
114 L. T. Duy, T. Q. Trung, V. Q. Dang, B.-U. Hwang, S. Siddiqui, I.-Y. Son, S. K. Yoon, D. J. Chung and N.-E. Lee, *Adv. Funct. Mater.*, 2016, **26**, 4329.
115 M. Hartwig, R. Zichner and Y. Joseph, *Chemosensors*, 2018, **6**, 66.
116 K. Kang, D. Yang, J. Park, S. Kim, I. Cho, H. H. Yang, M. Cho, S. Mousavi, K. H. Choi and I. Park, *Sens. Actuators, B*, 2017, **250**, 574.
117 O. Y. Kweon, M. Y. Lee, T. Park, H. Jang, A. Jeong, M.-K. Um and J. H. Oh, *J. Mater. Chem. C*, 2019, **7**, 1525.
118 B. Nketia-Yawson, A.-R. Jung, Y. Noh, G. S. Ryu, G. D. Tabi, K. K. Lee, B. S. Kim and Y. Y. Noh, *ACS Appl. Mater. Interfaces*, 2017, **9**, 7322.
119 M. S. Ansari, A. Banik, A. Kalita, P. K. Iyer and M. Qureshi, *J. Mater. Chem. A*, 2018, **6**, 15868.
120 O. Supplie, M. M. May, S. Brückner, N. Brezhneva, T. Hannappel and E. V. Skorb, *Adv. Mater. Interfaces*, 2017, 1601118.
121 X. L. Liu and M. C. Hersam, *Adv. Mater.*, 2018, **30**, 1801586.
122 L. Weinhardt, D. Hauschild and C. Heske, *Adv. Mater.*, 2019, **31**, 1806660.
123 J. J. Chen, X. H. Gao and D. G. Xu, *Adv. Mater. Sci. Eng.*, 2019, 5268267.